Genesis of the Shangxu orogenic gold deposit, Bangong-Nujiang suture belt, central Tibet, China: Constraints from H, O, C, Si, He and Ar isotopes

Xiang Fang [a,b,*], Juxing Tang [b], Yang Song [b,*], Georges Beaudoin [c,d], Chao Yang [c,d], Xiaowen Huang [e]

[a] Chinese Academy of Geological Sciences, Beijing 100037, China
[b] MNR Key Laboratory of Metallogeny and Mineral Assessment, Institute of Mineral Resources, Chinese Academy of Geological Sciences, Beijing 100037, China
[c] Department of Geology and Geological Engineering, Université Laval, Québec, QC G1V0A6, Canada
[d] Centre de recherche sur la géologie et l'ingénierie des ressources minérals (E4m), Québec, QC G1V0A6, Canada
[e] State Key Laboratory of Ore Deposit Geochemistry, Institute of Geochemistry, Chinese Academy of Sciences, Guiyang 550081, China

ABSTRACT

Shangxu is an orogenic gold deposit in the Bangong-Nujiang suture zone, central Tibet, China, formed in the Early Cretaceous orogene, related to convergence and collision between the Qiangtang and Lhasa terranes. The mineralization at Shangxu is hosted by Jurassic turbidite sedimentary rocks of the Mugagangri Group, and is associated with a regional fault system. Hydrothermal minerals develop muscovite, carbonate, sulfides and chlorite. Hydrothermal fluids record three main hydrothermal stages based on mineral paragenesis. The earliest is barren quartz stage (H1), which is pre-ore. During the early mineralization quartz-pyrite stage (H2a), defined by massive quartz veins with minor euhedral pyrite and gold, hydrothermal fluids had a $\delta^{18}O_{fluid}$ of 6.1–6.4‰, δD of −74 to −116‰, $\delta^{13}C_{CO2}$ of −5.4 to −7.6‰, and $\delta^{30}Si$ of −0.1‰. In the quartz-pyrite-sulfides stage (H2b), characterized by abundant quartz, granular pyrite, muscovite with minor chalcopyrite, galena, sphalerite and gold, fluids had a $\delta^{18}O_{fluid}$ of 7–8.2‰, δD of −109 to −120‰, $\delta^{13}C_{CO2}$ of −9.6‰ and $\delta^{30}Si$ of −0.1 to −0.2‰. During the ankerite-sulfide stage (H3a), distinguished by abundant ankerite, muscovite, sulfides with minor quartz and chlorite, hydrothermal system had a fluid with $\delta^{18}O_{fluid}$ of 4.9–5.3‰, δD of −125.3‰, $\delta^{30}Si$ of −0.1‰, $\delta^{13}C_{CO2}$ of −12.4‰ in quartz inclusion fluid and $\delta^{13}C_{CO2}$ of −2.7‰ in ankerite. The calcite-sulfide stage (H3b) is characterized by calcite, sulfides, with minor quartz and chlorite. Quartz formed earlier than calcite from a fluid having a $\delta^{18}O_{fluid}$ of 6.4‰, δD of −112.6‰, $\delta^{30}Si$ of −0.1‰, and $\delta^{13}C_{CO2}$ of −7.4‰, after which calcite precipitated from a hydrothermal fluid with $\delta^{18}O_{fluid}$ of 5.5–9‰, $\delta^{13}C_{CO2}$ of −0.5 to −2.8‰. Hydrothermal fluids in H2b pyrite have $^3He/^4He$ ratios of 0.27–0.42Ra and $^{40}Ar/^{36}Ar$ ratios of 313–372.

The stable isotope composition of hydrothermal fluids from the Shangxu gold deposit is similar to that of typical orogenic gold deposits. The early stage (H1), methane-bearing fluids were probably sourced from the basin sediments, leading to precipitation of early barren quartz veins and siderite alteration. From the quartz-sulfide stage (H2) to carbonate-sulfide stage (H3), hydrothermal fluids were likely derived from dissolution of the marine carbonate cement from sedimentary host rocks during metamorphism at depth. The decreasing δD and $\delta^{13}C$ of the ore-forming fluids from early to late suggests mixing with $\delta^{13}C$-depleted oxidized graphite in sedimentary rocks, meteoric waters or reation between δD-depleted organic matters. Generally, these fluids were likely generated at depth through prograde metamorphic devolatilization of hydrous minerals in the deeper equivalents of the sedimentary rocks of the Mugagangri Group. Sulfur and gold, by inference, likely originated from sedimentary/diagenetic pyrite or the metasedimentary rocks between the greenschist and amphibolite facies, and migrated with the metamorphic fluids. During transportation to the site of deposition, gold-bearing fluids variably reacted with country rocks.

1. Introduction

A number of Phanerozoic orogenic gold provinces are found in sedimentary rocks, particularly in turbidite sequences, such as in the Lachlan fold belt, Australia (Sandiford and Keays, 1986; Gao and Kwak, 1995; Phillips and Hughes, 1996; Bierlein et al., 1998, 2000), the Otago metamorphic terrane (McKeag and Craw, 1989; Craw, 2000; Pitcairn et al., 2006) and the Reefton goldfield in New Zealand (Christie and Brathwaite, 2002); the Meguma Terrane in Nova Scotia, Canada (Kontak et al., 1990; Ryan and Smith, 1998; Sangster et al., 2007); the Juneau gold belt in southern Alaska (Goldfarb et al., 1991); the Mother Lode goldfield in California (Boehlke and Kistler, 1986); and the Muruntau, Kumtor and Sawayaerdun gold deposits in the central Asian and southern Tianshan belt (Drew et al., 1996; Graupner et al., 2006; Chen et al., 2010, 2012a).

Gold has always been a main aim of mineral exploration along Bangong-Nujiang Suture Zone (BNSZ), Tibet (Tang et al., 2012; Song et al., 2014). More than 550 of gold occurrences and deposits have been found along this belt, including about 400 alluvial gold and 150 primary gold deposits/occurrences (Fig. 1; Li et al., 2017). Among them, gold-bearing porphyry copper mineralization dominates, such as Duolong and Ga'erqiong, which contain more than 20 million tonnage of Cu resources and 580 tonnage of Au resources (Tang et al., 2016, 2017), whereas the independent gold mines develop only a very few. Geological mapping and drilling from 2011 to 2013 in the central section of this metallogenic belt led to discovery of the Shangxu gold deposit and another two nearby gold prospects, Daze and Zuobu (Huang et al., 2014). Mineralization in this region is tectonically controlled by a regional fault system, and hosted by the Jurassic turbidite succession of the Mugagangri Group. The latter is considered to record deposition in an accretionary prism above the suture between the Qiangtang and Lhasa terranes (Pan et al., 2012; Metcalfe, 2013; Zeng et al., 2017).

Previous work on the deposit geology (Xiao et al., 2013; Huang et al., 2014), mineralogy and lithogeochemistry (Fang et al., 2020a), chronology (Fang et al., 2020b), fluid inclusion and stable isotopes (Pei et al., 2015, 2016; Xiao et al., 2017; Liu et al., 2018) of the Shangxu deposit identified that Shangxu is an orogenic gold deposit, formed in the Early Cretaceous orogene along the BNSZ. But the derivation of hydrothermal fluids and ore-forming materials still remain controversial. For instance, based on fluid inclusions and H-O isotopes of quartz, Pei et al. (2015) proposed a hydrothermal origin of metamorphic water mixing with formation/syngenetic water, and Xiao et al.(2017) considered a mixed source of metamorphic and meteoric water, whereas, Liu et al.(2018) surmised a deep mantle or magmatic reservoir, after studying C, S and Pb isotopes of the Shangxu deposit.

In order to better constrain the origin and evolution of hydrothermal fluids, an integrated stable isotope study of the Shangxu hydrothermal vein system is presented here. In this paper, we systematically sampled and analyzed O, H, C, and Si isotopes in hydrothermal quartz and carbonate from sub-stages of mineralization, measured the C isotope composition of graphite in sedimentary rocks and studied noble gases isotope (He-Ar) from fluid inclusions in pyrite. The isotopic data is used to propose a metallogenic model for the Shangxu deposit with implications for other sediment-hosted gold deposits in the Bangong-Nujiang Suture Zone.

2. Regional geologic setting

The Bangong-Nujiang Suture Zone (BNSZ) extends over 2000 km across the central Tibet and records the evolution of the Bangong-Nujiang Tethyan Ocean from the Permian to the Cretaceous. Regionally, the BNSZ separates the Qiangtang terrane to the north from the Lhasa terrane to the south (Fig. 1; Pan et al., 2012; Zhu et al., 2013), and is characterized by widely distributed ophiolitic fragments and thick successions of Jurassic flysch, melange, and volcanic rocks (Girardeau et al., 1984; Kapp et al., 2003; Geng et al., 2012, 2016; Pan et al., 2012; Metcalfe, 2013).

The Shangxu gold deposit is situated in the central section of the Bangong-Nujiang suture, approximately 40 km north-east of Nima city (Fig. 2A). Regionally, the Upper Triassic Quehala Group is the oldest formation, comprising a set of abyssal flysh sedimentary rocks. It is overlain by the Early to Middle Jurassic turbidite of the Mugagangri Group, which hosts the gold mineralization, comprised of interbedded greywacke, siltstone and carbonaceous slate. The Mugagangri Group is overlain by the Upper Jurassic Shamuluo Formation, composed of quartz sandstone, slate and interbedded limestone, the Lower Cretaceous Langshan Formation, consisting of limestone with minor intercalated siltstone and silty mudstone, in turn overlain by the Lower Cretaceous Qushenla Formation of fluvial and lacustrine sedimentary facies, consisting of sandstone, conglomerate, and interlayered andesite, the Upper Cretaceous Jingzhushan Formation of conglomerate and pebbly sandstone, and the Miocene Kangtuo Formation, composed of conglomerate, sandstone and minor basic volcanic rocks.

The Bangong-Nujiang Ocean probably closed during the Late Jurassic to the Early Cretaceous (~140–128 Ma, Kapp et al., 2003; Chen et al., 2004; Gao et al., 2011; Qu et al., 2012; Zhu et al., 2016; Fan et al., 2018; Song et al., 2019). Affected by convergence of the ocean basin, strong deformation occurred to the Mugagangri sedimentary rocks simultaneously (Liu et al., 2017b), leading to gold mineralization in the Shangxu region (~135 Ma, quartz Rb-Sr dating, Fang et al., 2020b).

Magmatic rocks, located about 20 km north of Shangxu, consist mainly of monzonitic granite, which is made up of alkali-feldspar,
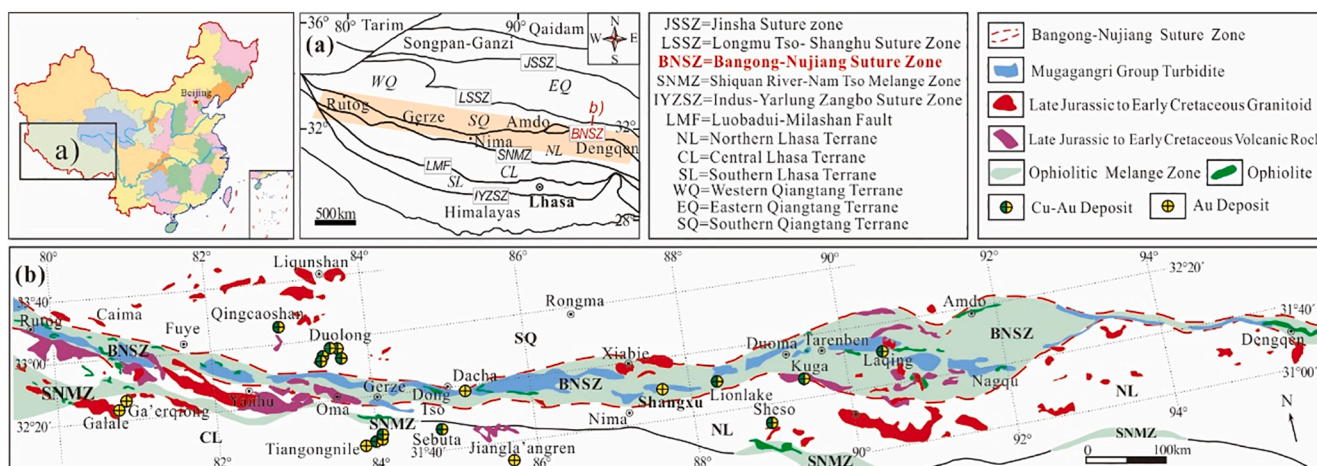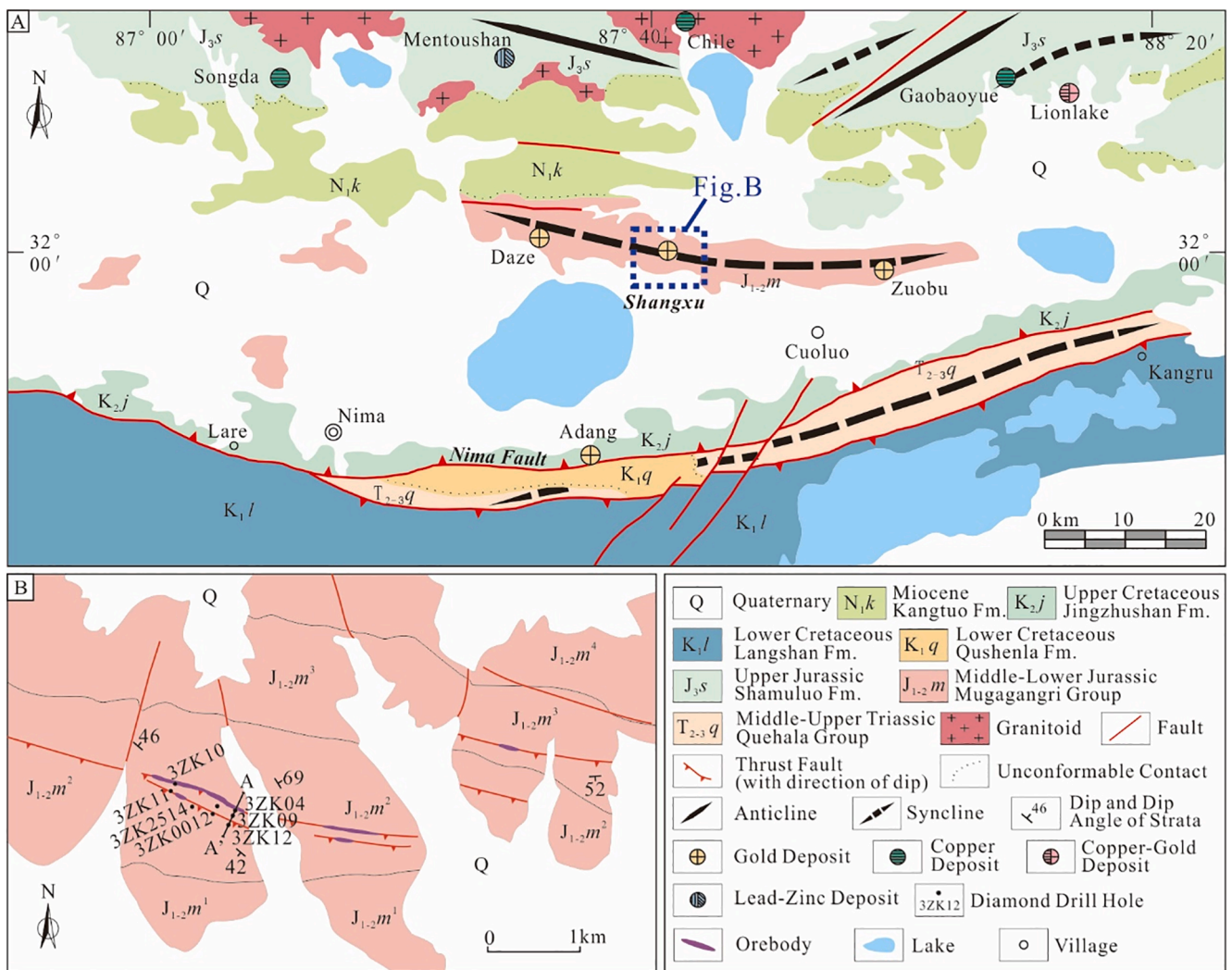

Fig. 1. Distribution of the major Au and Cu-Au deposits along the Bangong-Nujiang Suture Zone.

Fig. 2. Regional (A) and local geology (B) of the Shangxu gold deposit (modified from Kapp et al., 2007; Huang et al., 2014; Liu et al., 2017a; Xiao et al., 2017). The Mugagangri Group in the Shangxu ore field contains 4 lithologic members: $J_{1-2}m^1$-the first member, composed of greywackes interbeded with carbonaceous slates and limestone lenticles; $J_{1-2}m^2$-the second member, mainly composed of greywackes; $J_{1-2}m^3$-the third member, composed of greywackes interbedded with carbonaceous slates; $J_{1-2}m^4$-the fourth member, mainly composed of carbonaceous slates.

plagioclase, quartz and minor biotite, intruded during the Early Cretaceous, between 126 and 113 Ma (Kapp et al., 2007). The Cu, Au, Pb and Zn mineralization scattered around these granitoids are thought to have a magmatic origin (Huang et al., 2017). About 30 km north-east of Shangxu, a granodiorite dike crops out, with an intrusion age of 162–147 Ma, which is related to the Cu, Au mineralization in the Gaobaoyue region (Li, 2019).

3. Deposit geology

Mineralization in the Shangxu region is closely associated with faults and folds (Fig. 2B). Gold ores have a close spatial relationship with the regional Nima Fault, which is a part of the Rutog-Nima-Dongqen Fault, a first-order east to west crustal-scale thrust fault zone, defining the southern boundary of the Bangong-Nujiang Suture Zone (Geng et al., 2012). On the north side of this boundary, the subparallel faults are considered to be the branches of the Nima Fault, serving as regional controls on the lower order structures. The third-order thrust faults in the Shangxu goldfield strike approximately NWW and dip at 45°–80° to SSW, and the ductile deformation related to overthrusting are thought to coincide with gold mineralization (Huang et al., 2014). Geophysical surveys suggest these third-order gold bearing structures merge with a

second-order NNE-dipping shear zone at depth (Liu et al., 2017a), corresponding to the shortening and thickening of the accretionary prism after collision between the Lhasa and Qiangtang terranes (Kapp et al., 2007; Pan et al., 2012). Shangxu, Daze and Zuobu gold mines are all located in a regional syncline whose axis strikes NWW (Fig. 2A). The structural geometry in the Shangxu deposit is dominated by an anticline-syncline pair, which is transected by the SSW-dipping faults. The axial separation between the tight anticline and syncline is approximately 400 m and the fold axial surfaces are subvertical. The intersection of the fault feeder and fold, such as saddle reef, is a good place for gold to precipitate.

The Shangxu deposit contains 6 t Au (Huang et al., 2014). In the major lode zone, where the orebody strikes 290–300° and dip at 48–75° to the south, mineralization is composed of brecciated quartz and mixed clay-rich breccia matrix, which changes outwards into intensely deformed and sheared country rocks (Fig. 3). These sheared structures usually appear between competent and less competent lithological units, such that they are always brittle-fractured and composed of cataclasite, breccia and fault gouge (Fang et al., 2020a.). Foliation is marked by alignments of fine-grained muscovite and quartz, which typically form planar fabrics (Fig. 4A). Pressure solution and dissolution seams are well developed (Fig. 4B,C). Pyrite crystals with quartz pressure shadows are
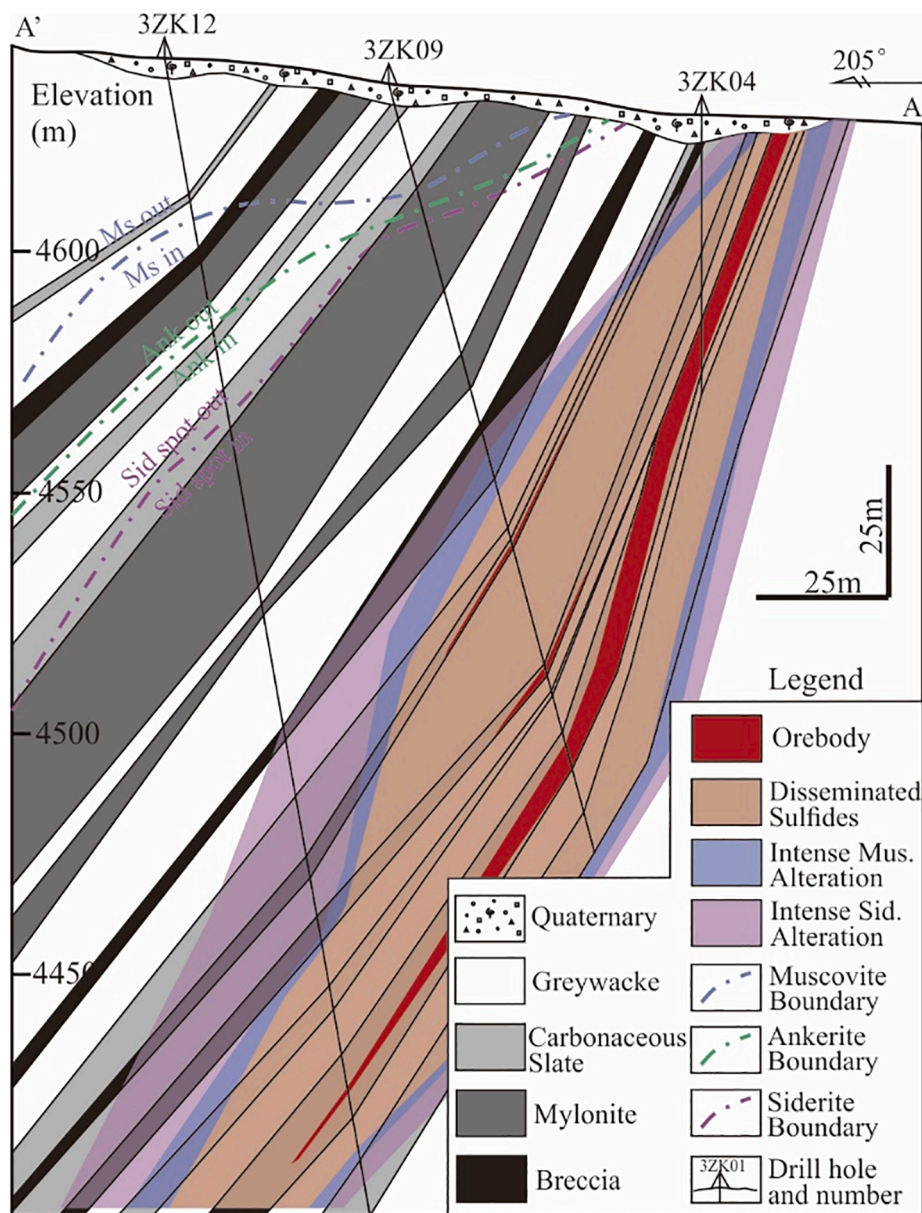
Fig. 3. Cross section (A-A′) of the Shangxu deposit, showing the location of drill holes and the overlapping alteration haloes surrounding the main auriferous lodes.

common in shear zones (Fig. 4D). Recrystallized, deformed and fibrous quartz grains are common (Fig. 4D–F). The mineral assemblage of sericite, quartz, carbonate and chlorite suggests a subgreenschist grade of metamorphism before gold mineralization.

Gold mineralization at Shangxu is principally hosted by massive to laminated quartz veins, saddle reefs, breccias and disseminated sulfides (Fang et al., 2020a). From proximal to distal to gold mineralization, wall rocks show hydrothermal alteration, including sulfidation, carbonatization, muscovitization and chloritization. Sulfide alteration is best developed within 20 m of the main auriferous lodes. Disseminated sulfides, nearby smaller quartz and carbonate veins, include pyrite, chalcopyrite, sphalerite, galena and minor marcasite, tetrahedrite, digenite, bornite, millerite, gersdorffite and cobaltite. Pyrite is the dominant mineral, typically representing more than 80% of the sulfides. More intense sulfidation is usually associated with gold mineralization, although it contains <5 vol% of sulfide minerals in both veins and disseminated mineralization. Carbonate porphyroblasts are composed of siderite that is partially to completely replaced by ankerite. These porphyroblasts form a halo around the main lode, which extends up to 70 m

away from the ore, decreasing in abundance outwards. Ankerite also forms veins or replaces feldspar and chlorite. The extent of the ankerite alteration halo is similar to that of the siderite, which spreads roughly 80 m far from the major ore. Calcite and dolomite veins cut quartz veins and ankerite grains locally. Hydrothermal muscovite develops proximal to the auriferous lode and subsidiary quartz ± carbonate veins within more than 10 m and decreases in abundance outwards to disappear within 100 m from the ore. They form aggregates in quartz ± carbonate vein and replacement of the wall rock matrix and rock fragments. Hydrothermal chlorite usually develops flaky texture in calcite veins and cracks. It's also found in wall rocks as replacement of the rock fragments.

4. Sampling

The sampling strategy was designed following the paragenetic sequences defined by previous workers and our study (Fig. 5). Barren quartz, related to the earliest hydrothermal activity (H1 stage), was not sampled. Three quartz-pyrite veins were sampled to represent the early mineralization stage (H2a). Three quartz-pyrite ± chalcopyrite ±
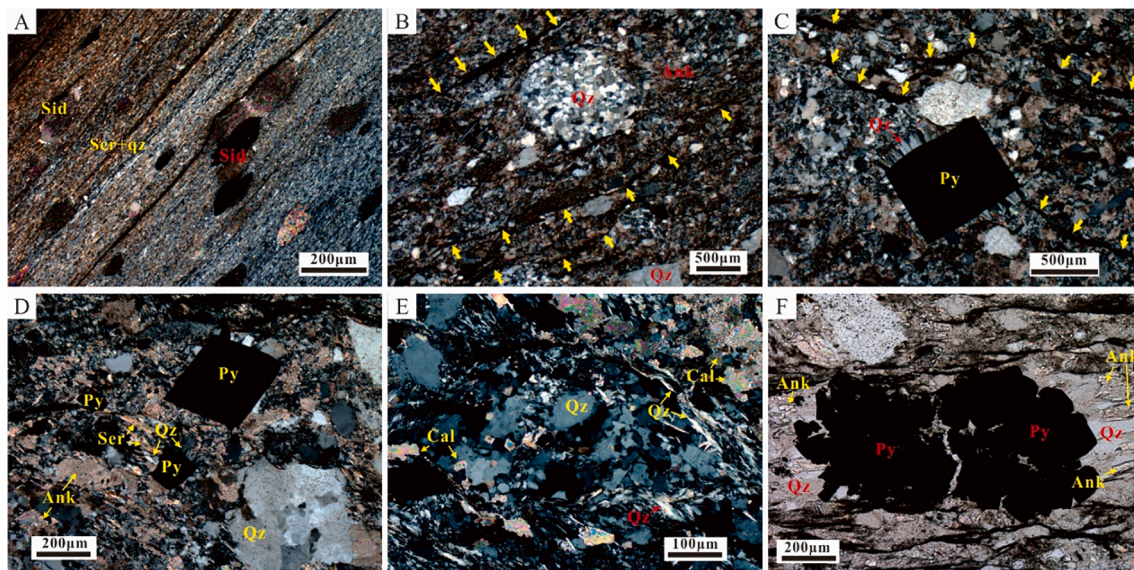
Fig. 4. Photomicrographs of structures at the Shangxu gold deposit. (A) planar fabrics of aligned sericite and quartz, overprinted by elongated and oriented siderite spots; (B) pressure solution and dissolution seams (yellow arrows) in host rocks; (C) pressure solution and dissolution seams (yellow arrows) and quartz pressure shadow around euhedral pyrite; (D) quartz subgrains and quartz pressure shadow around pyrite; (E) recrystallized and fibrous quartz grains; (F) quartz + ankerite pressure shadow around pyrite replaced by ankerite; Qz-quartz; Cal-calcite; Gra-graphite; Ser-sericite; Ank-ankerite; Sid-siderite; Py-pyrite.

galena ± sphalerite veins represent the middle mineralization stage (H2b). Two carbonate-quartz-sulfide veins and six calcite veins were selected to represent the late hydrothermal stage (H3a, H3b). In addition, six samples of graphite from wall rocks were selected for C isotope analysis. Five ore-related euhedral pyrite from the H2b stage and one pre-ore pyrite from the metamorphism stage were collected for He-Ar isotope measurements.

5. Analytical methods

Mineral separates were prepared from crushed and washed rock samples, followed by handpicking under a binocular microscope. Oxygen isotope analyses were carried out on 10 to 20 mg of quartz using the BrF_5 method, followed by quantitative conversion to CO_2 (Clayton and Mayeda, 1963). Hydrogen isotope composition of water, and carbon isotopes of CO_2, was measured from fluid inclusions decrepitated from quartz at 600 °C. The released gases passed through a CuO cup at 600 °C and were frozen with liquid nitrogen from which hydrogen gas was released by reduction with zinc (Coleman et al., 1982). CO_2 was collected, condensed and separated in a liquid nitrogen cooling trap for $\delta^{13}C$ analysis. $\delta^{18}O$ and $\delta^{13}C$ values for carbonate were measured on CO_2 released from 5 to 10 mg powdered carbonate samples reacted with 100% phosphoric acid (McCrea, 1950). Silicon was extracted from quartz separates using the fluorination technique following Taylor and Epstein (1962) and Jiang et al. (1994). The oxygen, hydrogen, silicon and carbon isotope ratios were measured using a Finnigan MAT 253EM mass spectrometer at the Analytical Laboratory in Beijing Research Institute of Uranium Geology, Beijing (ALBRIUG). The $\delta^{18}O$, $\delta^{13}C$, $\delta^{30}Si$ and δD values are reproducible to ±0.2‰, ±0.1‰, ±0.06‰ and ±2‰, respectively. The carbon isotopic composition of graphite was measured using a Thermo-Finnigan CF-IRMS with a precision of 0.2‰ at Queen's University, Canada. $\delta^{18}O$ and δD are reported relative to the Vienna-SMOW, $\delta^{13}C$ to the Vienna-PDB and $\delta^{30}Si$ to the NBS-28 quartz sandstone standard.

He and Ar gases of fluid inclusions in pyrite were extracted using a vacuum crushing method as described by Hu et al. (1998). Noble gas isotope analyses were performed with a Helix SFT noble gasses mass spectrometer at the Institute of Mineral Resources, Chinese Academy of Geological Sciences, Beijing. The sensitivity of the Helix SFT was >2 × 10^{-4} amps/Torr at 800 μA for He, and >1 × 10^{-3} amps/Torr at 200 μA

for Ar. The Faraday resolution is more than 400, and the resolution of the multiplier is greater than 700, allowing complete separation of ^3He and HD^+. The system blank was measured according to the same procedure for the sample analysis, and helium and argon blanks were below 2×10^{-11} cm³ STP and 1×10^{-10} cm³ STP respectively. Gas abundance was measured based on the atmosphere standard, with $^3He/^4He$ of 1.4 × 10^{-6} (Ra) and $^{40}Ar/^{36}Ar$ of 295.5.

6. Results

6.1. Vein mineralogy and paragenetic sequence

Mineralization at Shangxu evolved over three main hydrothermal stages, including a barren quartz stage (H1), a quartz-sulfide stage (H2) and a carbonate-sulfide stage (H3). The barren quartz stage (H1) is related to the formation of siderite spots, and usually contains no sulfide or gold (Fang et al., 2020a). The quartz-sulfide stage (H2) can be subdivided into a quartz-pyrite stage (H2a) and a quartz-pyrite ± chalcopyrite ± sphalerite ± galena stage (H2b). The quartz-pyrite stage (H2a) is defined as massive quartz and minor disseminated euhedral pyrite and gold (Fig. 6A). The H2b stage is characterized by abundant quartz, granular pyrite, muscovite with minor chalcopyrite, galena, sphalerite and gold (Fig. 6B). The carbonate-sulfide stage (H3) can be subdivided into an ankerite-sulfide stage (H3a) and a calcite-sulfide stage (H3b). The ankerite-sulfide stage (H3a) is defined by ankerite, muscovite, pyrite, galena, chalcopyrite and sphalerite, with minor quartz and chlorite (Fig. 6C,D). The calcite-sulfide stage (H3b) is dominated by calcite, pyrite, chalcopyrite, sphalerite and galena with minor quartz, chlorite, marcasite, bornite, digenite, tetrahedrite and millerite (Fig. 6E,F).

Previous studies recognized a barren quartz stage prior to mineralization, a quartz-pyrite stage and a quartz-polymetallic sulfide stage related to gold and a post-mineralization calcite-quartz stage (Pei et al., 2015; Xiao et al., 2017). Together with fluid inclusion and stabe isotope study, the evolution of fluid composition was determined (Table 1). Comparing with the previous paragenetic sequences, the quartz-pyrite stage and the quartz-polymetallic sulfide stage are integrated into the quartz-sulfide stage (H2) in this study. Previous study shows that the paragenetic evolution of this stage is continuous, with hydrothermal fluids evolving from relatively high temperature and salinity to lower values (Xiao et al., 2017), while similar mineral assemblages were being
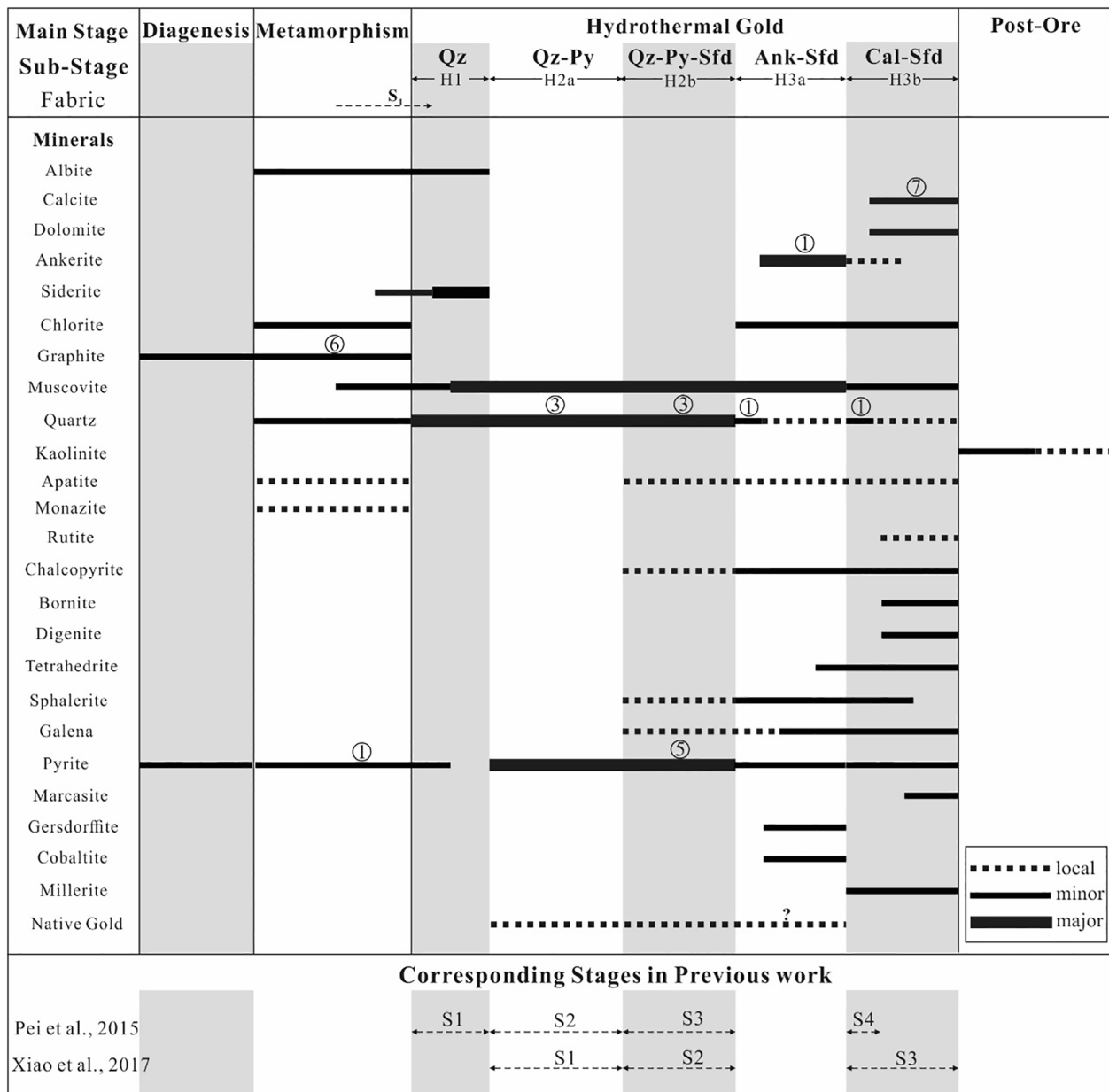
Fig. 5. Mineral paragenesis of the Shangxu gold deposit and its corresponding stage; the circled numbers above the mineral bars indicate the number of mineral samples from each sub-stage; Qz-quartz, Ank-ankerite, Cal-calcite, Py-pyrite; Sfd-sulfide.

precipitated (Fig. 5, Table 1). In addition, an ankerite-sulfide stage (H3a) is defined in this study. This is an important carbonate hydrothermal alteration associated with gold mineralization, postdating H2, which leads to pervasive ankerite alteration of country rocks. Calcite (H3b) dominates after the ankerite-sulfide stage.

6.2. $\delta^{18}O$, δD, $\delta^{13}C$ and $\delta^{30}Si$ of silicates

The range of quartz $\delta^{18}O$ value is between 16.7‰ and 19.5‰, with an average of 18.0‰ (Table 2, Fig. 7). $\delta^{18}O$ values of early mineralization quartz (H2a), H2b stage quartz and late-stage quartz (H3) range from 16.7‰ to 17‰, 18.1‰ to 19.3‰ and 18.4‰ to 19.5‰, with increasing mean values of 16.8‰, 18.7‰ and 19‰, respectively. The inclusion fluid δD values in quartz are between −74‰ and −125‰ with an average value −105‰ (Table 2). δD values of inclusion fluids from the early mineralized quartz (H2a) vary between −74 to -116‰ (average −88‰), H2b quartz range from −109 to -120‰ (average

−115‰,) and that for the late stage quartz (H3) ranges from −113 to −125‰ (average −119‰), respectively (Fig. 7). $\delta^{13}C$ values for inclusion fluid CO_2 in quartz show a gradual decrease from early mineralization quartz (H2a), −5.4‰ to −7.6‰, with an average of −6.5‰ (Table 2). The H2b quartz has a lower $\delta^{13}C_{CO2}$ value of −9.6‰, whereas the H3a and H3b quartz yields the $\delta^{13}C_{CO2}$ values of −12.4‰ and −7.4‰, respectively. The quartz silicon isotope composition is uniform with $\delta^{30}Si$ values of −0.1‰; one sample yields a lower value of −0.2‰ (Table 2, Fig. 8).

6.3. $\delta^{18}O$ and $\delta^{13}C$ of carbonates

The late-stage carbonates (H3) have relatively consistent $\delta^{18}O$ and $\delta^{13}C$ values (Table 2, Fig. 9). A H3a ankerite yields a $\delta^{18}O$ value of 16.5‰, similar to those of H3b calcite, which range from 16.5‰ to 20‰, with an average of 17.9‰. The $\delta^{13}C$ value of H3a ankerite is −1.3‰, comparable to those of the H3b calcite, which range from −0.1‰ to
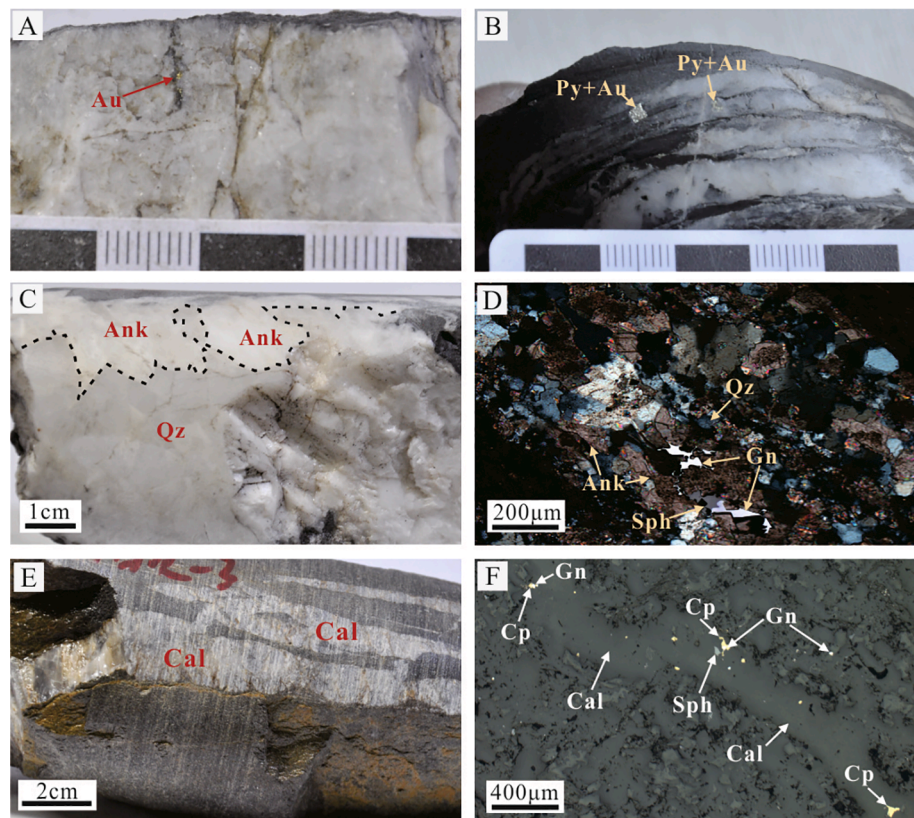
Fig. 6. Vein mineralogy of the Shangxu gold deposit. A. H2a stage quartz vein with gold grains in cracks; B. H2b stage laminated quartz vein with pyrite and gold in cracks; C. H3a stage ankerite-quartz vein; D. photomicrograph of an H3a stage ankerite- quartz- sphalerite- galena vein; E. H3b stage calcite veins; F. chalcopyrite, sphalerite and galena in a H3b stage calcite vein. Qz-quartz; Ank-ankerite; Cal-calcite; Au-native gold; Py-pyrite; Cp-chalcopyrite; Sph-sphalerite; Gn-galena.

Table 1
Paragenetic sequences and characteristics of hydrothermal fluids at Shangxu.

Reference	Pei et al. (2015)				Xiao et al. (2017)		
Group	S1	S2	S3	S4	S1	S2	S3
Definition	quartz stage (barren)	quartz-pyrite stage	quartz-sulfide polymetal stage	calcite-quartz stage	quartz-pyrite stage	quartz-sulfide polymetal stage	quartz-calcite stage
Dominated mineral	qz	qz, py, gl	qz, ms, py, cp, gn, sph, gl	cal, qz	qz, py, gl	qz, py, gn, sph, gl	cal, qz
Corresponding stage in this study	H1	H2a	H2b	H3b(partial)	H2a	H2b	H3b
FI type	L_l	$L_l + C_3 + C_2$	$L_l + L_v + C_3$		$L_l + L_v + C_3$	$L_l + C_3$	$L_l + L_v$
Th (ave.) °C	90–248 (144)	142–397 (235)	141–410 (247)		189–244 (218)	183–211 (208)	140–210 (180)
Satinity% NaCl eq.	0.35–5.86	3.06–9.74	2.74–8.68		3.87–10.98	1.57–9.34	2.07–3.57
Density g/cm³	0.85–0.98	0.61–0.96	0.55–0.97		0.87–0.96	0.85–0.93	0.87–0.93
Pressue MPa	5.4–21.6	11.6–40.4	10.3–39		16.11–24.83	12.25–20.52	11.26–15.37
D ‰	−99	−95 to -108	−89 to -102		−104 to -119	−108 to -136	
O$_{water}$ ‰	−0.8	2.3–5.8	0–5		5.92–7.82	4.92–5.32	

Qz-quartz, ms-muscovite, cal-calcite, ank-ankerite, py-pyrite, gl-gold, cp-chalcopyrite, gn-galena, sph-sphalerite; L_l- liquid fluid inclusion, L_v- vapor–liquid biphase fluid inclusion, C_2–CO_2-containing biphase fluid inclusion, C_3–CO_2-containing triphase fluid inclusion

−2.4‰, with a mean value of −1‰.

6.4. $\delta^{13}C$ of graphite

The graphite carbon isotope composition is uniform, with a narrow range of $\delta^{13}C$ value between −20.8‰ and −21.3‰, with a mean value of −21.0‰ (Table 2).

6.5. He-Ar isotope of inclusion fluids in pyrite

Analytical results for He and Ar are listed in Table 3. The concentrations of ^4He range from 35.88–101.01 × 10^{-8} cm³STP/g for all

analyzed samples. $^3He/^4He$ ratios of the ore-related H2b samples vary between 0.27Ra and 0.42Ra with a pre-ore sample from the metamorphism stage of a $^3He/^4He$ value 1.03Ra (where Ra is the $^3He/^4He$ ratio of air, 1.4 × 10^{-6}). The $^{40}Ar/^{36}Ar$ ratios are between 308.8 and 532.3. The ratios of $^3He/^{36}Ar$ show the greatest variability, ranging from 460.74 × 10^{-7} to 12636.31 × 10^{-7}. The F^4He values are the ratios of $^4He/^{36}Ar$ in samples and in atmosphere, which provide a good estimate of the atmospheric He contribution to the sample fluids (Kendrick et al., 2001), ranging from 509.87 to 5276.59. The concentrations of ^{40}Ar range from 30.14–222.17 × 10^{-8} cm³STP/g for all fluids in pyrite and the $^{40}Ar*/^4He$ ratios (radiogenic ^{40}Ar) are from 0.11 to 0.27, similar to the crustal $^{40}Ar*/^4He$ production ratios of 0.2.

Table 2
Oxygen, hydrogen, silicon and carbon isotopic compositions of quartz, inclusion fluids, carbonate and graphite from the Shangxu deposit.

Sample	Mineral	Position	Stage	$\delta^{18}O_{V\text{-}SMOW}$ (‰)		$\delta^{13}C_{V\text{-}PDB}$ (‰)			$\delta D_{V\text{-}SMOW}$ (‰)	$\delta^{30}Si_{NBS\text{-}28}$ (‰)
				Qz	Cal/Ank	Qz	Cal/Ank	Gr	Qz FI	Qz
K08-159	Qz + Ank	Vein	H3a	18.4	16.5	−12.4	−1.3		−125.3	−0.1
K11-184	Qz + Cal	Vein	H3b	19.5	19.2	−7.4	−0.1		−112.6	−0.1
SX1-1	Qz	Vein	H2a	16.7					−74.6	−0.1
SX2-Q1	Qz	Vein	H2a	16.8		−7.6			−74.2	−0.1
401–34	Qz	Vein	H2a	17		−5.4			−116.2	−0.1
514–242	Qz	Vein	H2b	19.3					−120.4	−0.1
012–62	Qz	Vein	H2b	18.1					−109.1	−0.2
012–61	Qz	Vein	H2b			−9.6				
K07-123	Cal	Vein	H3b		17.9		−1			
Y12-18	Cal	Vein	H3b		16.9		−2.4			
514–111	Cal	Vein	H3b		17.7		−0.8			
012–260	Cal	Vein	H3b		16.5		−1.2			
012–175	Cal	Vein	H3b		20		−0.3			
012–261	Cal	Vein	H3b		17.4		−1.2			
k12-350	Gr	Host rock						−21		
k12-195	Gr	Host rock						−21.3		
k12-202	Gr	Host rock						−21.1		
K11-119	Gr	Host rock						−20.8		
K 10-72	Gr	Host rock						−21		
k2514-212	Gr	Host rock						−21.1		

Qz-quartz, Ank-ankerite, Cal-calcite; Gr-graphite; FI-fluid inclusion.
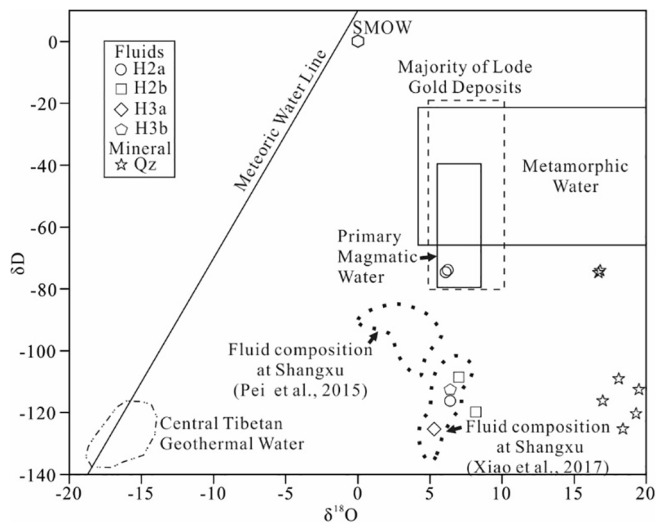

Fig. 7. δD and $\delta^{18}O$ values of hydrothermal fluids from the Shangxu gold deposit. Field for magmatic and metamorphic waters is from Taylor and Barnes (1997); the central Tibetan geothermal water is from Zheng et al. (1982); majority of the lode gold deposits is from McCuaig and Kerrich (1998); fluid composition at Shangxu from Pei et al. (2015) and Xiao et al. (2017).

7. Discussion

7.1. Temperature of the hydrothermal process

At Shangxu, different types of fluid inclusions in auriferous quartz (H2a, H2b) are characterized by coexisting CO_2-rich triphase and liquid-rich biphase inclusions (Pei et al., 2015; Xiao et al., 2017). The homogenization temperature (T_h) of the two inclusion types is similar, and the salinity of the CO_2-rich fluid inclusions is generally lower than those of the liquid-rich fluid inclusions (Xiao et al., 2017). These observations were interpreted to indicate immiscibility or boiling when the quartz veins formed, and the homogenization temperature approximates the trapping temperature (Lu et al., 2004). Accordingly, we use the average T_h from Xiao et al. (2017) to represent the hydrothermal fluid temperatures during H2a and H2b stages (218 °C and 208 °C, respectively). Pei et al. (2016) calculated a T_t of 197 °C by S isotope sphalerite-galena fractionation for the H2b stage, consistent with the H2b average homogenization temperature of 208 °C.

Using Zheng (1999), the quartz-ankerite and quartz-calcite oxygen isotope fractionations yield temperatures of 127 °C and 823 °C, respectively. The latter high temperature is far from the temperature range measured from fluid inclusions, suggesting isotopic disequilibrium between quartz and calcite in that sample (*k*11-184). The low temperature is compatible with the T_h range of H3 stage (140–210 °C, Xiao et al., 2017). It is similar to T_h (152–293 °C) from turbidite-hosted deposits in the Buller Terrane, New Zealand, where hydrothermal
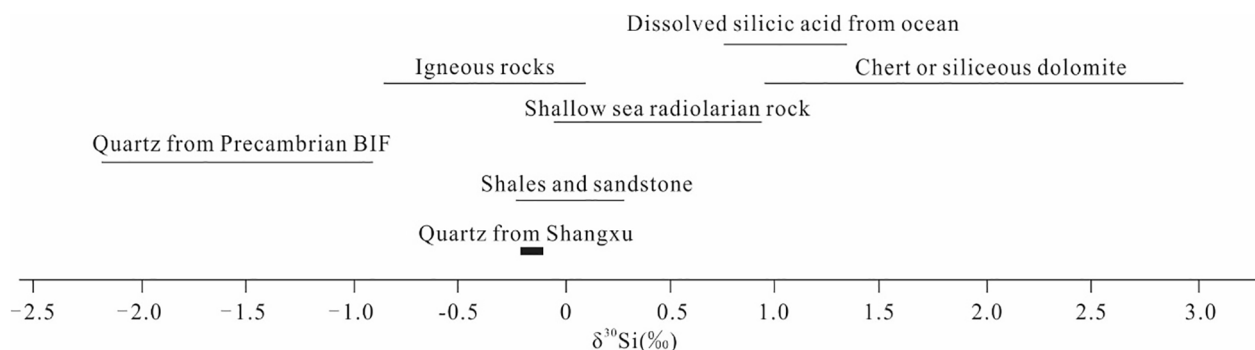
Fig. 8. Silicon isotopic composition of quartz from the Shangxu gold deposit. The major reservoirs for silicon are from Chen et al. (2012a) and Poitrasson (2017).
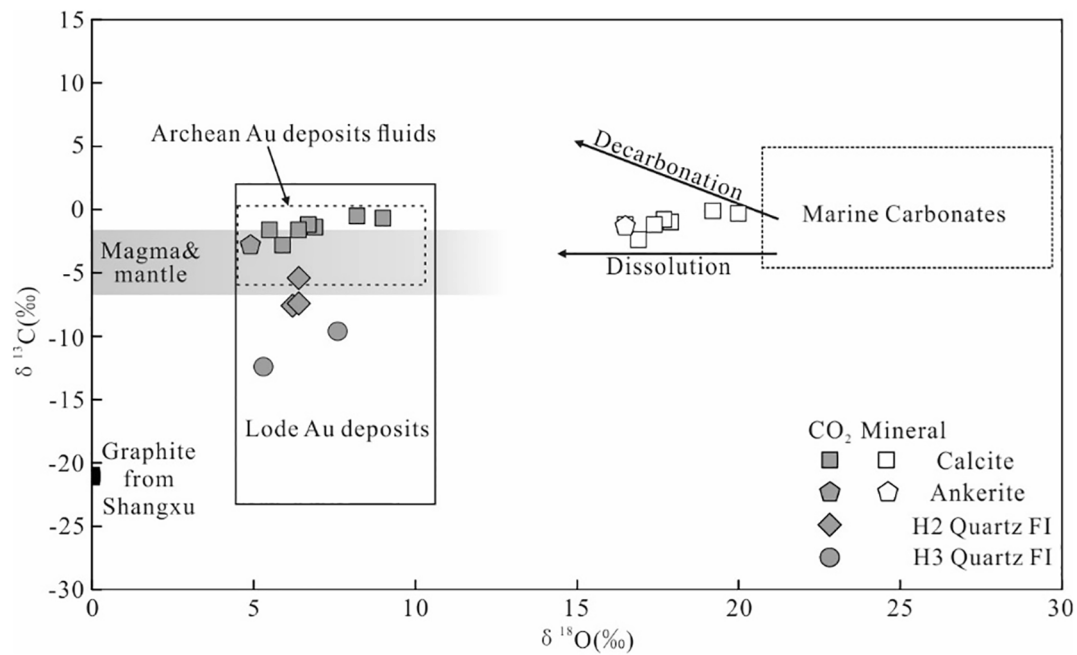
Fig. 9. $\delta^{13}C$ and $\delta^{18}O$ values of mineral and CO_2 in fluids from the Shangxu gold deposit. Field for lode gold deposits is from McCuaig and Kerrich (1998); Archean gold deposits is from Ridley and Diamond (2000); marine carbonate is from Ohmoto and Rye (1979); magmatic and mantle carbon is from Deines et al. (1991); evolution trends for dissolution and decarbonation are from Shieh and Taylor (1969) and Ohmoto and Goldhaber (1997).

Table 3
Helium and argon isotopic data from fluid inclusions in pyrite from the Shangxu gold deposit.

Samples	Forming stage	$^3He/^4He$ (10^{-7})	^4He $(10^{-8}\ cm^3STP/g)$	R/Ra	$^{40}Ar/^{36}Ar$	^{40}Ar $(10^{-8}\ cm^3STP/g)$	$^{40}Ar*/^4He$	$^3He/^{36}Ar$ (10^{-7})	F^4He
k12-198	ore-stage	4.53	35.88	0.32	341.4	30.14	0.11	1841.07	2455.70
k12-143	ore-stage	3.78	58.47	0.27	372.4	35	0.12	2351.62	3759.04
k11-124	pre-ore	14.47	101.01	1.03	532.3	61.57	0.27	12636.31	5276.59
514–208	ore-stage	5.92	78.49	0.42	308.8	222.17	0.12	645.84	659.19
514–217	ore-stage	4.77	66.89	0.34	330.2	103.34	0.16	1019.50	1291.43
514–212	ore-stage	5.46	54.77	0.39	313.3	203.35	0.21	460.74	509.87

$F^4He = (^4He/^{36}Ar)_{sample}/(^4He/^{36}Ar)_{air}$, $^4He/^{36}Ar$ in air is 0.1655; $^{40}Ar*$ refers to the superfluous-argon after deducting the ^{40}Ar in air, $^{40}Ar* = (^{40}Ar)_{sample}295.5 \times (^{36}Ar)_{sample}$.

alteration haloes are dominated by carbonate, sericite, chlorite and sulfide alteration (Bierlein et al., 2004). During H3 stage, where fluid inclusions within a single fluid inclusion assemblage have similar volatile phase ratios, homogenization temperature is considered the minimum estimate of the trapping temperature. Thus, we use the average T_h (180 °C) from Xiao et al. (2017) to represent the hydrothermal fluid temperature during H3 stage.

7.2. Composition and origin of the hydrothermal fluid

Several hypotheses for the origin of the hydrothermal fluids in orogenic gold deposits have been proposed: (1) metamorphic devolatilization of hydrous and carbonate minerals during prograde metamorphism (Kerrich and Fyfe, 1981; Phillips and Nooy, 1988; Barnicoat et al., 1991; Kerrick and Caldeira, 1998), (2) fluids evolved from devolatilization of magma (Burrows et al., 1986; Burrows and Spooner, 1987), (3) metal-rich fluid sourced from mantle degassing (Groves et al., 1988), or from melts formed in the metasomatic sub-continental lithospheric mantle (Hronsky et al., 2012), (4) deep meteoric water circulation (Nesbitt, 1988; Menzies et al., 2014).

7.2.1. Water composition
Auriferous quartz $\delta^{18}O$ values from the Shangxu gold deposit range from 16.7‰ to 19.5‰, δD values range from −74.2‰ to −125.3‰, and

carbonates $\delta^{18}O$ values range from 16.2 to 20‰ (Table 2), consistent with those of the typical orogenic lode gold deposits (Fig. 7; Kyser et al., 1986; Goldfarb et al., 1991; Goldfarb, 1997; McCuaig and Kerrich, 1998; Jia et al., 2000, 2001; Kerrich et al., 2000; Kerrich et al., 2000; Ridley and Diamond, 2000; Beaudoin, 2011). The relatively high $\delta^{18}O$ values are consistent with a low ore-forming temperature which would lead to significant isotopic fractionation between the fluid, mineral and sedimentary host rocks (O'Neil, 1986; Beaudoin, 2011; Chen et al., 2012b). Using Clayton et al. (1972), the calculated $\delta^{18}O$ of hydrothermal fluids in quartz of H2a ranges from 6.1‰ to 6.4‰ (average 6.2‰). δD values of inclusion fluids from H2a quartz vary between −74 and −116‰ (average −88‰). This $\delta^{18}O$ and δD composition may reflect either a magmatic or a metamorphic water source. Similarly, $\delta^{18}O$ of hydrothermal fluids in quartz from H2b and H3 stage are calculated to be 7–8.2‰ (average 7.6‰) and 5.3–6.4‰ (average 5.9‰), respectively. The $\delta^{18}O$ of water in equilibrium with carbonate, using the ankerite-water and calcite-water fractionations of Zheng (1999), yield $\delta^{18}O_{H2O}$ values of 4.9‰ and from 5.5‰ to 9‰ (average 6.9‰), respectively. The calculated $\delta^{18}O_{H2O}$ values of hydrothermal fluids at Shangxu, from 4.9‰ to 9‰, are comparable to that for the most gold lodes deposits worldwide ($\delta^{18}O = 5$–16‰; Boehlke and Kistler, 1986; Goldfarb et al., 1991; Kontak and Kerrich, 1995; Oberthuer et al., 1996; Bierlein and Crowe, 2000; Jia et al., 2003; Beaudoin, 2011). δD values of inclusion fluids from H2b and H3 are −109 to -120‰ (average −115‰) and −113

to -125‰ (average −119‰), respectively (Table 2). Combined with δD data from Pei et al. (2015) and Xiao et al. (2017), the integrated dataset shows decreasing δD values from H2a to H3 (Fig. 7), approaching to the composition of central Tibetan geothermal water (Zheng et al., 1982). It is likely that the high topography during uplift of the Tibetan Plateau promoted penetration of meteoric water into the rock pile, analogous to that happening in the present-day Alpine schists, New Zealand (Koons, 1987; Koons and Craw, 1991; Pitcairn et al., 2006). Hence, the low δD values (<80‰) could be interpreted to indicate mixing with meteoric water (Beaudoin, 2011), consistent with the low T_h in the district. The low δD values could also result from extraction of fluids from several generations of inclusions. The fact that there is a gradual decrease in δD from H2 to H3 is not consistent with this hypothesis. On the other hand, reaction between δD-depleted organic matter in host rocks could also cause the low δD signature (Goldfarb et al., 1989; McCuaig and Kerrich, 1998; Jia et al., 2001; Wong et al., 2017). Craw (2002) argued the low δD value in hydrothermal fluid could result from graphite deposition during mineralization, due to exchange with CH_4-rich reduced fluids in shear zones. But in the Shangxu gold deposit, CH_4 is not a dominant phase in hydrothermal fluids and graphite is not an abundant accessory mineral in the host rocks for gold veins.

7.2.2. Source for silicon

According to previous work, silicon isotopes will not be significantly partitioned during water–rock interaction (Douthitt, 1982; Ding et al., 1994), so silicon isotope can be used to identify the source of hydrothermal fluids in different ore deposits (Jiang et al., 1993, 1994; Zhou et al., 2007; Chen et al., 2012b). The $\delta^{30}Si$ values of quartz at Shangxu are restricted to the interval −0.1 to -0.2‰, with a mean of −0.11‰, within the range of shales and sandstones, or igneous rocks, but distinctly different from those of Precambrian Banded Iron Formations or shallow sea radiolarian rocks (Fig. 8). To distinguish contributions of water from shales and sandstones versus water from igneous rocks based on merely measured silicon isotope values is difficult. However, if combined with the foregoing high $\delta^{18}O$ signature of quartz veins from the Shangxu deposit, the sedimentary rock source is plausible.

7.2.3. Sources of carbon

The $\delta^{13}C_{CO2}$ values in quartz veins are low, ranging from −5.4 to −12.4‰, similar to the range of −3 to −12‰ for the Bendigo goldfield in Australia (Cox et al., 1995; Gao and Kwak, 1995; Phillips and Hughes, 1996), the Cambrian-Ordovician turbidite-hosted gold deposit of Muruntau in Uzbekistan and the Carbonaceous phyllite-hosted gold deposit of Kumtor in Kyrgyzstan (−5 to −12‰, Drew et al., 1996; Ivanov et al., 2000), and the carbon isotope composition for global orogenic gold veins from the Archean to the Cenozoic (−26 to 13‰, with most values at modes of −5‰ and −22‰, Beaudoin, 2011). A magmatic or mantle degassing carbon source fails to fully account for the gold-bearing quartz stage at the Shangxu deposit, because the $\delta^{13}C$ range exceeds that of the magma and mantle (Fig. 9).

The $\delta^{13}C$ value of hydrothermal carbonate at Shangxu ranges from −0.1 to −2.4‰, with an average of −1.0‰, which corresponds to seawater carbon (0‰, Ohmoto and Rye, 1979). Dissolution or decarbonation reactions of carbonate during metamorphism produce CO_2 with $\delta^{13}C$ values similar to, or more enriched in $\delta^{13}C$, than that in parent rocks (Shieh and Taylor, 1969; Ohmoto and Goldhaber, 1997). $\delta^{13}C$ values of CO_2 calculated from calcite range from −0.5 to −2.8‰ (average −1.4‰), based on the calcite-CO_2 fractionation of Ohmoto and Rye (1979). To calculate the $\delta^{13}C$ values of CO_2 from ankerite, we use the fractionation for dolomite-CO_2 (Ohmoto and Rye, 1979) as an approximation to that of ankerite-CO_2. The calculated $\delta^{13}C_{CO2}$ in equilibrium with ankerite is −2.7‰, similar to that for calcite. Collectively, the calculated $\delta^{13}C_{CO2}$ display a small range from −0.5 to −2.8‰, similar to those of fluids forming the Archean gold deposits (−6 to 0‰, McCuaig and Kerrich, 1998; Ridley and Diamond, 2000). In conjunction with the $\delta^{18}O$ values, Fig. 9 illustrates dissolution of the marine

carbonates is the most likely source of carbon.

The $\delta^{13}C$ values of graphite in sediments within the Shangxu district are around −21‰ (Table 2). The spread $\delta^{13}C$ values of CO_2 in quartz fluid inclusions, between the local graphite and marine carbonate composition (Fig. 9), could be interpreted to indicate mixing of isotopically depleted oxidized graphite in sedimentary rocks with the carbonic species originating from disseminated marine carbonate cement from the sedimentary host rocks.

7.2.4. He-Ar isotope

Pyrite is regarded as a good trap for noble gases and previous studies have shown that loss of He and Ar from pyrite fluid inclusions is negligible on a 100 Ma time scale (Burnard et al., 1999). The composition of fluids trapped in quartz is similar to that in pyrite where quartz is intergrown with pyrite during the same ore stage (Hu et al., 1998). In our study, all samples were collected from drill holes such that cosmogenic ^3He production in mineral lattice and fluid inclusions can be ignored (Simmons et al., 1987; Stuart et al., 1995; Burnard et al., 1999). Since Li-bearing minerals are absent from the Shangxu deposit, a source of ^4He through radioactive decay of lithium can also be excluded. The F^4He values, the $^4He/^{36}Ar$ ratio of samples relative to the atmospheric $^4He/^{36}Ar$ value of 0.1655, reflect contribution from atmospheric He, and a sample with 100% atmospheric He has an F value of unity (Kendrick et al., 2001; Li et al., 2007). All F^4He values of our pyrite samples are greater than 1, suggesting that atmospheric He is negligible. In addition, He contents in atmosphere are too low to influence the He abundance and isotopic composition of crustal fluids (Marty et al., 1993; Stuart et al., 1994), such that He isotopic composition of hydrothermal fluids reflects the original signature.

In the ^3He vs. ^4He correlation diagram, pyrite samples plot in a field close to the crust (Fig. 10A), and the R/Ra ratios can be used to trace source of helium contained in hydrothermal fluids. The value for mantle He (R_m) ranges from 6 to 7 Ra (Dunai and Baur, 1995; Stuart et al., 1995), whereas that of crustal fluids (R_c) typically ranges from 0.01 to 0.05 Ra (Tolstikhin, 1978). In our study, the R/Ra values (R_s) of H2b samples range from 0.27 to 0.42, with a relatively high value of 1.03 of the pre-ore metamorphic sample. This R/Ra range is lower than that of mantle, and typical of crustal fluids. The R/Ra ratios can also be used to estimate the proportion of mantle and crustal components in fluids. Using a value of 6 Ra to represent pure mantle He (R_m), and 0.03 Ra as typical crustal fluids (R_c), a proportion of mantle He between 4 and 6.6% for the H2b samples and a higher mantle He content of 16.8% for the pre-ore metamorphic sample (k11-124) are estimated with the equation $He_{mantle} = (R_s-R_c)/(R_m-R_c) \times 100\%$. This indicates that He in the fluid inclusions in pyrite mainly came from a crustal source.

The $^{40}Ar/^{36}Ar$ values of fluid inclusion in pyrite range from 309 to 532. Compared with the atmospheric ratio (298), the higher $^{40}Ar/^{36}Ar$ ratios of samples indicate a higher concentration of radiogenic ^{40}Ar ($^{40}Ar^*$) of mantle or crustal origin. The $^{40}Ar^*/^4He$ ratios of samples range between 0.11 and 0.27, close to crustal production ratio of 0.2 (Stuart et al., 1995), indicating the inheritance of Ar from the crustal components. In the R/Ra vs. $^{40}Ar^*/^4He$ (Fig. 10B) and R/Ra vs. $^{40}Ar/^{36}Ar$ diagram (Fig. 10C), the samples constitute a well-defined correlation similar to the Daduhe (east Tibet, China) and Jinshan (Jiangxi, east China) gold deposits, where hydrothermal fluids have a large crustal component (Li et al., 2007, 2010), suggesting the dominance of crust-derived fluids in the Shangxu gold mineralization process. In the $^{40}Ar/^{36}Ar$ vs. 3He/36Ar plot (Fig. 10D), the composition of Shangxu hydrothermal fluids coincides with the metamorphic water line, consistent with that of the Muruntau gold deposit.

The pre-ore sample k11-124, with a relatively larger mantle component, is comparable to the gold deposits in the Jiaodong peninsula, China, where gold mineralization is interpreted to have a relatively high proportion of mantle fluids (Shen et al., 2013; Goldfarb and Santosh, 2014; Goldfarb and Groves, 2015). This might reflect more magmatic activities prior to mineralization during metamorphism in the
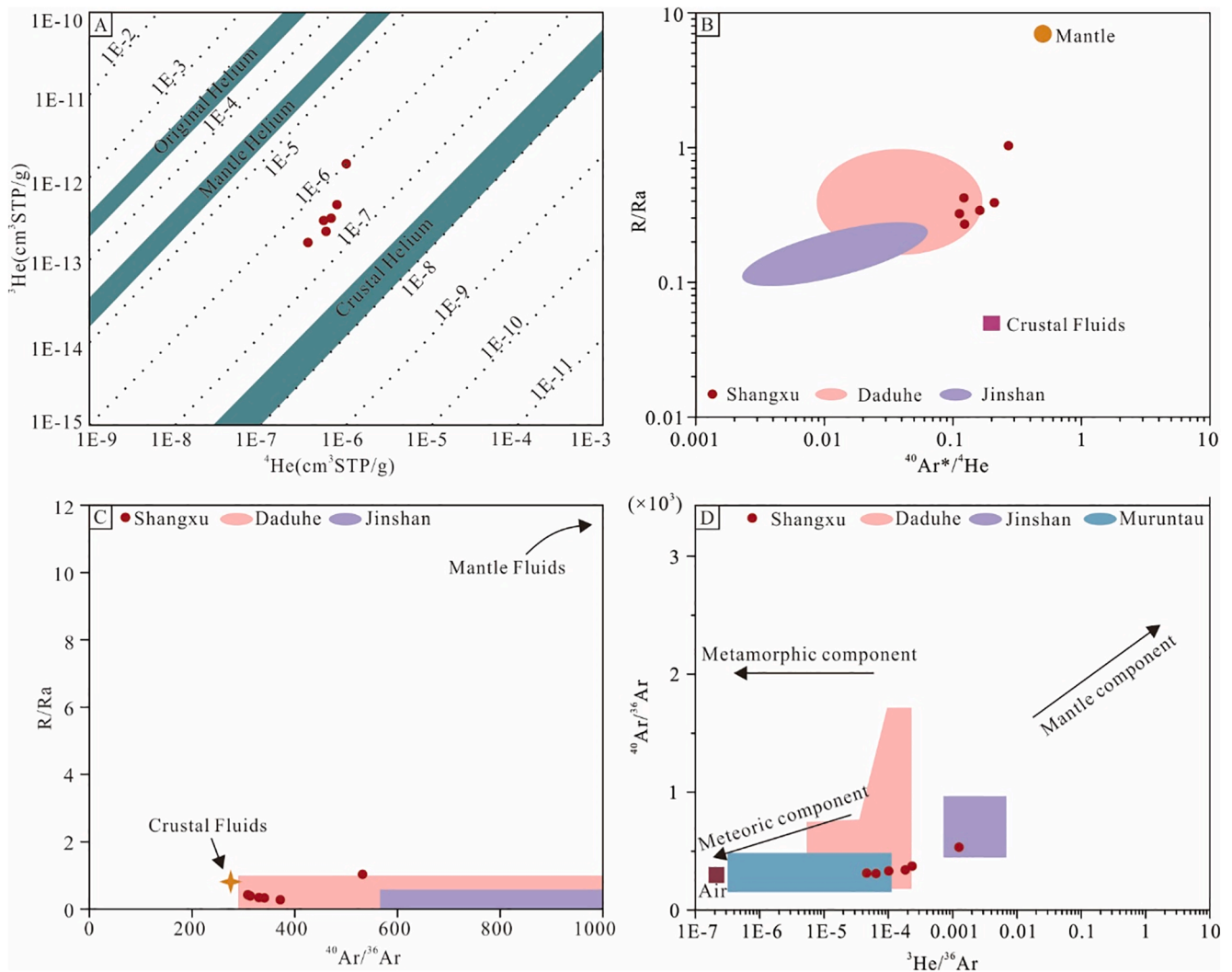
Fig. 10. (A) $^{40}Ar/^{36}Ar$ vs. $^{3}He/^{36}Ar$, (B) ^{3}He vs. ^{4}He, (C) $^{40}Ar*/^{4}He$ vs. R/Ra and (D) $^{40}Ar/^{36}Ar$ vs. R/Ra diagrams for fluid inclusions in pyrite (modified after Hu et al., 1998; Mao et al., 2002; Li et al., 2010). Data sources: Murantau Au depoist (Graupner et al., 2006), Daduhe Au deposits (Li et al., 2007), Jinshan Au deposit (Li et al., 2010).
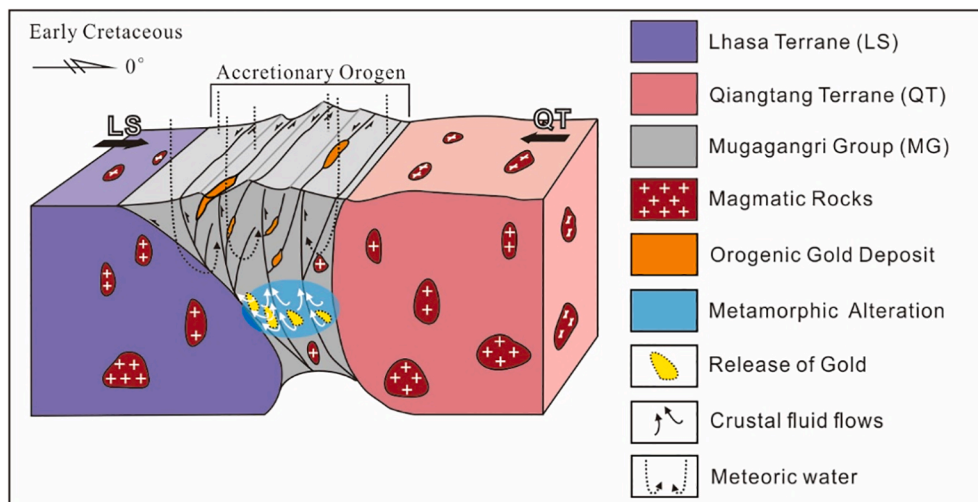
Fig. 11. Genetic model for the Shangxu gold deposit, see text for detailed explanation.

Shangxu region, or leaking up the fault from the depth.

7.3. Fluid evolution and ore genesis

The turbidites of the Mugagangri Group were deposited along the sourthern Qiangtang continental margin (Zeng et al., 2017). The high gold background (14.32 ppb Au) of the regional slates and greywackes suggests a sedimentary enrichment in gold (Xiao, 2002; Deng et al., 2015; Zeng et al., 2017). Gold could have been trapped in organic matter or in diagenetic/sedimentary pyrite (Large et al., 2015). In the Early Cretaceous orogene, convergence and accretion between the Qiangtang and Lhasa terranes, followed by strike-slip movement, caused extensive crustal compression and thickening in the fore-arc region along the continental margin (Fig. 11).

At this time, due to deformation in the fore-arc turbiditic sedimentary sequences, burial to the depth induced prograde metamorphism, as shown by the hydrothermal fluid's $^{40}Ar/^{36}Ar$ and $^3He/^{36}Ar$ composition (Fig. 10D), and the low R/Ra and $^{40}Ar*/^4He$ ratios. The earliest hydrothermal fluids (H1) were barren in gold, and formed the siderite spot alteration. These fluids are interpreted to be derived from the basin sediments and are commonly methane-bearing (Irwin et al., 1977; Welhan, 1988; Hinrichs et al., 1999; Whiticar, 1999; Boetius et al., 2000; Dugdale et al., 2009). Auriferous fluids infiltrated the Mugagangri Formation after the siderite alteration. Gold-bearing hydrothermal flows (H2) were likely produced by breakdown of hydrous minerals, such as chlorite, in sedimentary rocks during greenschist to amphibolite facies metamorphic reactions (Elmer et al., 2006; Fyfe, 2012; Pitcairn et al., 2014; Goldfarb and Groves, 2015). After migrating along the Bangong-Nujiang crustal scale shear zone, quartz and pyrite precipitated from a moderate temperature (>220 °C), low salinity, CO_2-rich fluid (H2a), which had a $\delta^{18}O_{fluid}$ of 6.1–6.4‰, δD of −74.2 to −−116.2‰, $\delta^{13}C_{CO2}$ of −5.4 to −7.6‰, and $\delta^{30}Si$ of −0.1‰.

With progressive crustal uplift and erosion, and progressive development of strike-slip faults caused cooling in hydrothermal fluids from H2a to H2b. Consequently, the hydrothermal fluids forming H2b stage, rich in CO_2, incorporated CO_2 from oxidization of graphite and from dissolution of carbon from disseminated marine carbonate in turbidite. Precipitation of quartz, pyrite as well as minor chalcopyrite, galena, sphalerite from a solution with $\delta^{18}O_{fluid}$ of 7–8.2‰, δD of −109.1 to −120.4‰, $\delta^{13}C_{CO2}$ of −9.6‰ and $\delta^{30}Si$ of −0.1‰ to −0.2‰ formed stage H2b.

Following the main mineralization stage, uplift resulted in progressive cooling of the metamorphic hydrothermal fluids. Disseminated marine carbonate dissolved by auriferous fluids became a major source of carbon to the fluids. Hydrothermal stage H3a evolved to form massive ankerite, quartz, sulfides from a fluid with a $\delta^{18}O_{fluid}$ of 4.9–5.3‰, δD of −125.3‰, $\delta^{30}Si$ of −0.1‰, $\delta^{13}C_{CO2}$ of −12.4‰ in quartz inclusion fluid and $\delta^{13}C_{CO2}$ of −2.7‰ in ankerite-CO_2. Crosscutting of quartz by ankerite suggests that quartz formed slightly before ankerite, which coincides with a change of the $\delta^{13}C$ value. With temperature decrease, calcite, quartz and sulfides, without gold, started to precipitate from a lower temperature (<180 °C), low salinity hydrothermal stage H3b. $\delta^{18}O$ and $\delta^{13}C$ between H3b quartz and calcite are in disequilibrium, and the crosscutting of quartz by calcite suggests quartz formed before calcite. The H3b quartz formed from a fluid having a $\delta^{18}O_{fluid}$ of 6.4‰, δD of −112.6‰, $\delta^{30}Si$ of −0.1‰, $\delta^{13}C_{CO2}$ of −7.4‰, whereas calcite deposited from a fluid with $\delta^{18}O_{fluid}$ of 5.5–9‰, $\delta^{13}C_{CO2}$ of −0.5 to -2.8‰.

Based on sulfur and lead isotopes of the Shangxu deposit, Pei et al. (2016) proposed an ore-forming materials source from the flysch sediments of the Mugagangri Group, whereas Liu et al. (2018) argued for a mixed origin of deep crustal-mantle magma and overlying flysch sediments. Their studies reached to a consistent sulfide $\delta^{34}S$ range, with diagenetic pyrite $\delta^{34}S$ of −3.1–2.2‰ and hydrothermal sulfides of −4.5–4.6‰ (Pei et al., 2016; Liu et al., 2018). The $\delta^{34}S$ of the Early to Middle Jurassic seawater sulfate varied mostly between 14 and 18‰

(Claypool et al., 1980; Canfield, 2004; Kampschulte and Strauss, 2004; Paytan and Gray, 2012), while the $\delta^{34}S$ values of sulfides in deposits were typically 15–20‰ lower than the coeval seawater sulfate (Chang et al., 2008). Thus, diagenetic pyrite in the Mugagangri Group was most probably derived from seawater sulfate, and leached from pyrite with S isotope compositions around 0‰, which is similar to that of magmatic sulfides. According to this study, contributions from magma and mantle were limited. Hence, sulfur and gold, by inference, were most likely released from diagenetic pyrite during conversion from pyrite to pyrrhotite at depth (Ferry, 1981; Large et al., 2011) or moblized from the sedimentary rocks at the greenschist to amphibolite transition (Pitcairn et al., 2014).

8. Conclusions

A stable isotopic study of hydrothermal minerals of the Shangxu gold deposit leads to the following conclusions:

(1) $\delta^{18}O$ and δD of hydrothermal fluids is compatible with metamorphic water, mixing with meteoric water, or reacting with δD-depleted organic matter in host rocks.

(2) Carbonic species in hydrothermal fluids from gold-bearing quartz stage (H2) were sourced from the dissolved marine carbonate cement, which mixed with depleted oxidized graphite in sedimentary rocks. During H3 stage, dissolution of the marine carbonate cement became the main source of carbon.

(3) He and Ar isotopes in hydrothermal pyrite inclusion fluids imply a major crustal origin.

The stable isotope compositions of hydrothermal fluids at Shangxu are comparable to those of typical orogenic gold deposits. The stable isotope systematics (O, H, C, Si, He and Ar) provide a constraint on source reservoirs of hydrothermal fluids in the Shangxu gold deposit. Hydrothermal ore-forming fluids probably formed due to Early Cretaceous orogeny and sourced from the depth, by devolatilization related to breakdown of hydrous minerals in the sedimentary rocks.

Declaration of Competing Interest

The authors declare that they have no known competing financial interests or personal relationships that could have appeared to influence the work reported in this paper.

Acknowledgment

Appendix A. Supplementary data

Supplementary data to this article can be found online at https://doi.org/10.1016/j.oregorev.2020.103810.

References

Barnicoat, A.C., Fare, R.J., Groves, D.I., McNaughton, N.J., 1991. Synmetamorphic lode-gold deposits in high-grade Archean settings. Geology 19 (9), 921–924.

Beaudoin, G., 2011. The stable isotope geochemistry of orogenic gold deposits. In: 11th SGA Biennial Meeting, pp. 556–558.

Bierlein, F., Arne, D., McKnight, S., Lu, J., Reeves, S., Besanko, J., Marek, J., Cooke, D., 2000. Wall-rock petrology and geochemistry in alteration halos associated with mesothermal gold mineralization, central Victoria, Australia. Econ. Geol. 95 (2), 283–311.

Bierlein, F., Christie, A., Smith, P., 2004. A comparison of orogenic gold mineralisation in central Victoria (AUS), western South Island (NZ) and Nova Scotia (CAN): implications for variations in the endowment of Palaeozoic metamorphic terranes. Ore Geol. Rev. 25, 125–168.

Bierlein, F., Crowe, D., 2000. Phanerozoic orogenic lode gold deposits. In: Hagemann, S. G., Brown, P.E. (Eds.), Gold in 2000, Reviews in Economic Geology, pp. 103–139.

Bierlein, F., Fuller, T., Stüwe, K., Arne, D., Keays, R., 1998. Wallrock alteration associated with turbidite-hosted gold deposits. Examples from the Palaeozoic Lachlan Fold Belt in central Victoria, Australia. Ore Geol. Rev. 13 (1–5), 345–380.

Boehlke, J.K., Kistler, R., 1986. Rb-Sr, K-Ar, and stable isotope evidence for the ages and sources of fluid components of gold-bearing quartz veins in the northern Sierra Nevada foothills metamorphic belt, California. Econ. Geol. 81 (2), 296–322.

Boetius, A., Ravenschlag, K., Schubert, C.J., Rickert, D., Widdel, F., Gieseke, A., Amann, R., Jørgensen, B.B., Witte, U., Pfannkuche, O., 2000. A marine microbial consortium apparently mediating anaerobic oxidation of methane. Nature 407 (6804), 623.

Burnard, P.G., Hu, R., Turner, G., Bi, X.W., 1999. Mantle, crustal and atmospheric noble gases in ailaoshan gold deposits, Yunnan Province, China. Geochim. Cosmochim. Acta 63 (10), 1595–1604.

Burrows, D., Wood, P., Spooner, E., 1986. Carbon isotope evidence for a magmatic origin for Archaean gold-quartz vein ore deposits. Nature 321 (6073), 851.

Burrows, D.R., Spooner, E., 1987. Generation of a magmatic H2O-CO2 fluid enriched in Au, Mo, and W within an Archean sodic granodiorite stock, Mink Lake, northwestern Ontario. Econ. Geol. 82 (7), 1931–1957.

Canfield, D., 2004. The evolution of the earth surface sulfur reservoir. Am. J. Sci. 304, 839–861.

Chang, Z., Large, R.R., Maslennikov, V., 2008. Sulfur isotopes in sediment-hosted orogenic gold deposits: evidence for an early timing and a seawater sulfur source. Geology 36 (12), 971–974.

Chen, G., Liu, H., Jiang, G., Zeng, Q., Zhao, S., Zhang, X., 2004. Discovery of the Shamuluo Formation in the central segment of the Bangong Co- Nujiang River suture zone, Tibet. Geol. Bull. China 23 (2), 193–194 (in Chinese with English abstract).

Chen, H., Chen, Y., Baker, M.J., 2012a. Evolution of ore-forming fluids in the Sawayaerdun gold deposit in the Southwestern Chinese Tianshan metallogenic belt, Northwest China. J. Asian Earth Sci. 49, 131–144.

Chen, H., Chen, Y., Baker, M., 2012b. Isotopic geochemistry of the Sawayaerdun orogenic-type gold deposit, Tianshan, northwest China: implications for ore genesis and mineral exploration. Chem. Geol. 310, 1–11.

Chen, X., Peng, R., Liu, J., Wang, J., Wang, X., 2010. Geological characteristics of Kumtor super large gold deposit in Kyrgyzstan. Gold 31 (12), 15–19 (in Chinese with English Abstract).

Christie, A.B., Brathwaite, R.L., 2002. Hydrothermal alteration in metasedimentary rock-hosted orogenic gold deposits, Reefton goldfield, South Island, New Zealand. Mineral. Deposita 38 (1), 87–107.

Claypool, G.E., Holser, W.T., Kaplan, I.R., Sakai, H., Zak, I., 1980. The age curves of sulfur and oxygen isotopes in marine sulfate and their mutual interpretation. Chem. Geol. 28, 199–260.

Clayton, R.N., Mayeda, T.K., 1963. The use of bromine pentafluoride in the extraction of oxygen from oxides and silicates for isotopic analysis. Geochim. Cosmochim. Acta 27 (1), 43–52.

Clayton, R.N., O'Neil, J.R., Mayeda, T.K., 1972. Oxygen isotope exchange between quartz and water. J. Geophys. Res. 77 (17), 3057–3067.

Coleman, M.L., Shepherd, T.J., Durham, J.J., Rouse, J.E., Moore, G.R., 1982. Reduction of water with zinc for hydrogen isotope analysis. Anal. Chem. 54 (6), 993–995.

Cox, S., Sun, S., Etheridge, M., Wall, V., Potter, T., 1995. Structural and geochemical controls on the development of turbidite-hosted gold quartz vein deposits, Wattle Gully mine, central Victoria, Australia. Econ. Geol. 90 (6), 1722–1746.

Craw, D., 2000. Fluid flow at fault intersections in an active oblique collision zone, Southern Alps, New Zealand. J. Geochem. Explor. 69, 523–526.

Craw, D., 2002. Geochemistry of late metamorphic hydrothermal alteration and graphitisation of host rock, Macraes gold mine, Otago Schist, New Zealand. Chem. Geol. 191 (4), 257–275.

Deines, P., Harris, J.W., Gurney, J.J., 1991. The carbon isotopic composition and nitrogen content of lithospheric and asthenospheric diamonds from the Jagersfontein and Koffiefontein kimberlite, South Africa. Geochim. Cosmochim. Acta 55 (9), 2615–2625.

Deng, J., Lu, X., Zhong, J., Wan, C., Yuan, Z., Du, C., Zhong, W., 2015. Sedimentary Basin Analysis and Tectonic Evolution of the Early-Middle Jurassic Mugagangri Group in Kangtuo Area, Tibet. Geol. Surv. China 2 (6), 34–41 (in Chinese with English abstract).

Ding, T., Jiang, S., Wan, D., Li, Y., 1994. In: Silicon Isotope Geochemistry. Geological Publishing House, Beijing, China, pp. 1–120 (in Chinese with English Abstract).

Douthitt, C.B., 1982. The geochemistry of the stable isotopes of silicon. Geochim. Cosmochim. Acta 46 (8), 1449–1458.

Drew, L.J., Berger, B.R., Kurbanov, N.K., 1996. Geology and structural evolution of the Muruntau gold deposit, Kyzylkum desert, Uzbekistan. Ore Geol. Rev. 11 (4), 175–196.

Dugdale, A.L., Wilson, C.J.L., Leader, L.D., Robinson, J.A., Dugdale, L.J., 2009. Carbonate spots: understanding the relationship to gold mineralization in Central Victoria, southeastern Australia. Miner. Deposita 44 (2), 205–219.

Dunai, T.J., Baur, H., 1995. Helium, neon, and argon systematics of the European subcontinental mantle: implications for its geochemical evolution. Geochim. Cosmochim. Acta 59 (13), 2767–2783.

Elmer, F., White, R., Powell, R., 2006. Devolatilization of metabasic rocks during greenschist–amphibolite facies metamorphism. J. Metamorph. Geol. 24 (6), 497–513.

Fan, J., Li, C., Wang, M., Xie, C., 2018. Reconstructing in space and time the closure of the middle and western segments of the Bangong-Nujiang Tethyan Ocean in the Tibetan Plateau. Int. J. Earth Sci. 107 (1), 231–249.

Fang, X., Tang, J., Beaudoin, G., Song, Y., Chen, Y., 2020a. Geology, mineralogy and geochemistry of the Shangxu orogenic gold deposit, central Tibet, China: implications for mineral exploration. Ore Geol. Rev. https://doi.org/10.1016/j.oregeorev.2020.103440.

Fang, X., Song, Y., Tang, J., Wang, J., Li, H., 2020b. Metallogenetic epoch study on the Shangxu gold deposit, Bangong-Nujiang Suture Zone, Tibet and its geological implications. Acta Geol. Sin. https://doi.org/10.19762/j.cnki.dizhixuebao.2020168 (in Chinese with English Abstract).

Ferry, J.M., 1981. Petrology of graphitic sulfide-rich schists from south-central Maine: an example of desulfidation during prograde regional metamorphism. Am. Mineral. 66 (9–10), 908–930.

Fyfe, W.S., 2012. In: Fluids In The Earth's Crust: Their Significance In Metamorphic, Tectonic And Chemical Transport Process. Elsevier, p. 377.

Gao, S., Zheng, Y., Wang, J., Zhang, Z., Yang, C., 2011. The geochronology and geochemistry of intrusive rocks in Bange area: constraints on the evolution time of the Bangong Lake-Nujiang ocean basin. Acta Petrol. Sin. 27 (7), 1973–1982 (in Chinese with English Abstract).

Gao, Z., Kwak, T., 1995. Turbidite-hosted gold deposits in the Bendigo-Ballarat and Melbourne Zones, Australia. I. Geology, Mineralization, stable isotopes, and implications for exploration. Int. Geol. Rev. 37 (10), 910–944.

Geng, Q., Peng, Z., Zhang, Z., Pan, G., Wang, L., Guan, J., Jia, B., Diao, Z., 2012. Tethyan Evolution and Geological Background of the Bangong Co-Nujiang Metallogenetic Zone and Adjacent Region. Geological Publishing House (in Chinese).

Geng, Q., Zhang, Z., Peng, Z., Guan, J., Zhu, X., Mao, X., 2016. Jurassic-Cretaceous granitoids and related tectono-metallogenesis in the Zapug-Duobuza arc, western Tibet. Ore Geol. Rev. 77, 163–175.

Girardeau, J., Marcoux, J., Allegre, C., Bassoullet, J., Youking, T., Xuchang, X., Yougong, Z., Xibin, W., 1984. Tectonic environment and geodynamic significance of the Neo-Cimmerian Donqiao ophiolite, Bangong-Nujiang suture zone, Tibet. Nature 307 (5946), 27.

Goldfarb, R., 1997. Gold deposits in metamorphic rocks of Alaska: implications for ore genesis. Econ Geol. Monogr. 9, 151–190.

Goldfarb, R.J., Groves, D.I., 2015. Orogenic gold: common or evolving fluid and metal sources through time. Lithos 233, 2–26.

Goldfarb, R.J., Leach, D.L., Rose, S.C., Landis, G.P., 1989. Fluid inclusion geochemistry of gold-bearing quartz veins of the Juneau gold belt, southeastern Alaska: implications for ore genesis. Econ. Geol. Monogr. 6, 363–375.

Goldfarb, R.J., Newberry, R.J., Pickthorn, W.J., Gent, C.A., 1991. Oxygen, hydrogen, and sulfur isotope studies in the Juneau gold belt, southeastern Alaska; constraints on the origin of hydrothermal fluids. Econ. Geol. 86 (1), 66–80.

Goldfarb, R.J., Santosh, M., 2014. The dilemma of the Jiaodong gold deposits: are they unique? Geosci. Front. 5 (2), 139–153.

Graupner, T., Niedermann, S., Kempe, U., Klemd, R., Bechtel, A., 2006. Origin of ore fluids in the Muruntau gold system: constraints from noble gas, carbon isotope and halogen data. Geochim. Cosmochim. Acta 70 (21), 5356–5370.

Groves, D., Golding, S., Rock, N., Barley, M., McNaughton, N., 1988. Archaean carbon reservoirs and their relevance to the fluid source for gold deposits. Nature 331 (6153), 254.

Hinrichs, K.-U., Hayes, J.M., Sylva, S.P., Brewer, P.G., DeLong, E.F., 1999. Methane-consuming archaebacteria in marine sediments. Nature 398 (6730), 802.

Hronsky, J.M., Groves, D.I., Loucks, R.R., Begg, G.C., 2012. A unified model for gold mineralisation in accretionary orogens and implications for regional-scale exploration targeting methods. Miner. Deposita 47 (4), 339–358.

Hu, R., Burnard, P.G., Turner, G., Bi, X., 1998. Helium and Argon isotope systematics in fluid inclusions of Machangqing copper deposit in west Yunnan province, China. Chem. Geol. 146 (1), 55–63.

Huang, H., Li, G., Liu, B., Zhang, Z., Ma, D., Qu, Z., Xiao, W., Liu, H., 2014. Discovery of Shangxu orogenic type gold deposit in northern Tibet and its significance. Miner. Deposits 33 (3), 486–496 (in Chinese with English abstract).

Huang, H., Liu, H., Zhang, L., Jiao, Y., Ouyang, Y., Ma, D., Cao, H., Zhang, Z., Zhang, H., Ma, G., Hou, C., Wu, J., and Zhang, H., 2017, Report of Geological Survey and Evaluation on Shangxu Gold Deposit, Shuanghu, Tibet. Geological report: Chengdu Geological Survey Center, China Geological Suvey (in Chinese).

Irwin, H., Curtis, C., Coleman, M., 1977. Isotopic evidence for source of diagenetic carbonates formed during burial of organic-rich sediments. Nature 269 (5625), 209.

Ivanov, S.M., Ansdell, K.M., Melrose, D.L., 2000. Ore texture and stable isotope constraints on ore deposition mechanisms at the Kumtor lode gold deposit. In: Bucci, L.A., Mair, J.L. (eds.), Gold in 2000: Lake Tahoe-Reno, Nevada, Centre for global metallogeny, University of Western Austirlia, v. Extended Abstract Volume, pp. 47–52.

Jia, Y., Kerrich, R., Goldfarb, R., 2003. Metamorphic origin of ore-forming fluids for orogenic gold-bearing quartz vein systems in the North American Cordillera: constraints from a reconnaissance study of δ 15N, δ D, and δ 18O. Econ. Geol. 98 (1), 109–123.

Jia, Y., Li, X., Kerrich, R., 2000. A fluid inclusion study of Au-bearing quartz vein systems in the central and north Deborah deposits of the Bendigo gold field, central Victoria, Australia. Econ. Geol. 95 (3), 467–494.

Jia, Y., Li, X., Kerrich, R., 2001. Stable isotope (O, H, S, C, and N) systematics of quartz vein systems in the turbidite-hosted Central and North Deborah gold deposits of the Bendigo gold field, central Victoria, Australia: constraints on the origin of ore-forming fluids. Econ. Geol. 96 (4), 705–721.

Jiang, S., Ding, T., Wan, D., Li, Y., 1993. Silicon isotopic compositions of Archean banded Si-Fe formation (BIF) in the Gongchangling ore deposit, Liaoning Province, China. Sci. China Seri. B-Chem., Life Sci. Earth Sci. 36 (4), 482–489.

Jiang, S., Palmer, M.R., Ding, T., Wan, D., 1994. Silicon isotope geochemistry of the Sullivan Pb-Zn deposit, Canada; A preliminary study. Econ. Geol. 89 (7), 1623–1629.

Kampschulte, A., Strauss, H., 2004. The sulfur isotopic evolution of Phanerozoic seawater based on the analysis of structurally substituted sulfate in carbonates. Chem. Geol. 204 (3), 255–286.

Kapp, P., DeCelles, P.G., Gehrels, G.E., 2007. Geological records of the Lhasa-Qiangtang and Indo-Asian collisions in the Nima area of central Tibet. GSA Bull. 119 (7–8), 917–933.

Kapp, P., Murphy, M.A., Yin, A., Harrison, T.M., Ding, L., Guo, J., 2003. Mesozoic and Cenozoic tectonic evolution of the Shiquanhe area of western Tibet. Tectonics 22 (4), 1–24.

Kendrick, M.A., Burgess, R., Pattrick, R.A.D., Turner, G., 2001. Fluid inclusion noble gas and halogen evidence on the origin of Cu-Porphyry mineralising fluids. Geochim. Cosmochim. Acta 65 (16), 2651–2668. https://doi.org/10.1016/S0016-7037(01)00618-4.

Kerrich, R., Fyfe, W.S., 1981. The gold—carbonate association: Source of CO2, and CO2 fixation reactions in Archaean lode deposits. Chem. Geol. 33 (1), 265–294. https://doi.org/10.1016/0009-2541(81)90104-2.

Kerrich, R., Goldfarb, R., Groves, D., Garwin, S., Jia, Y., 2000. The characteristics, origins, and geodynamic settings of supergiant gold metallogenic provinces. Sci. China Seri. D: Earth Sci. 43 (1), 1–68.

Kerrich, D.M., Caldeira, K., 1998. Metamorphic CO2 degassing from orogenic belts. Chem. Geol. 145 (3), 213–232.

Kontak, D.J., Kerrich, R., 1995. Geological and geochemical studies of a metaturbidite-hosted lode gold deposit; the Beaver Dam Deposit, Nova Scotia; II, Isotopic studies. Econ. Geol. 90 (4), 885–901.

Kontak, D.J., Smith, P.K., Kerrich, R., Williams, P.F., 1990. Integrated model for Meguma Group lode gold deposits, Nova Scotia, Canada. Geology 18 (3), 238–242.

Koons, P.O., 1987. Some thermal and mechanical consequences of rapid uplift: an example from the Southern Alps, New Zealand. Earth Planet. Sci. Lett. 86 (2), 307–319.

Koons, P.O., Craw, D., 1991. Gold mineralization as a consequence of continental collision: an example from the Southern Alps, New Zealand. Earth Planet. Sci. Lett. 103 (1), 1–9.

Kyser, T.K., Janser, B.W., Wilson, M.R., Hattie, I., 1986. Stable isotope geochemistry related to gold mineralization and exploration in the Western Shield: Gold in the Western Shield. CIM Spec. 38, 470–498.

Large, R.R., Bull, S.W., Maslennikov, V.V., 2011. A carbonaceous sedimentary source-rock model for carlin-type and orogenic Gold deposits. Econ. Geol. 106 (3), 331–358.

Large, R.R., Gregory, D.D., Steadman, J.A., Tomkins, A.G., Lounejeva, E., Danyushevsky, L.V., Halpin, J.A., Maslennikov, V., Sack, P.J., Mukherjee, I., Berry, R., Hickman, A., 2015. Gold in the oceans through time. Earth Planet. Sci. Lett. v. 428, 139–150.

Li, H., 2019. Diagenesis and metallogenesis of Late Jurassic adakitic rocks in the Gaobaoyue area, Tibet. Doctoral Thesis: China University of Geosciences, Beijing (in Chinese with English Abstract).

Li, Y., Huang, H., Liu, H., Lu, M., Lan, S., 2017. Gold mineralization in the Bangong-Nujiang metallogenic zone, Tibet: sedimentary Geology and Tethyan. Geology 37 (2), 1–13 (in Chinese with English Abstract).

Li, X., Mao, J., Wang, C., Watanabe, Y., 2007. The Daduhe gold field at the eastern margin of the Tibetan Plateau: He, Ar, S, O, and H isotopic data and their metallogenic implications. Ore Geol. Rev. 30 (3), 244–256.

Li, X., Wang, C., Hua, R., Wei, X., 2010. Fluid origin and structural enhancement during mineralization of the Jinshan orogenic gold deposit, South China. Mineral. Deposita 45 (6), 583–597.

Liu, H., Li, G., Huang, H., Xiao, W., Yan, G., Ma, D., Zhang, H., Zhang, H., 2018. Sources of Ore-forming materials in the Shangxu Orogenic Gold Deposit, Northern Xizang (Tibet): constraints from C, S and Pb isotopes. Geol. Rev. 64 (5), 1285–1301 (in Chinese with English Abstract).

Liu, H., Li, G., Huang, H., Zhang, Z., Xiao, W., Jiao, Y., Liang, S., Guo, J., Lan, S., 2017a. Prospecting potential analysis of deep No. 3 ore section in the Shangxu Orogenic Gold Deposit, Bangong Co-Nujiang Metallogenic Belt, Tibet. Acta Geol. Sin. 91 (6), 1245–1258 (in Chinese with English Abstract).

Liu, Y., Wang, M., Li, Y., Xie, C., Chen, H., Li, Y., Fan, J., Li, X., Xu, W., Sun, Z., 2017b. Cretaceous structures in the Duolong region of central Tibet: evidence for an accretionary wedge and closure of the Bangong-Nujiang Neo-Tethys Ocean. Gondwana Res. 48, 110–123.

Lu, H., Fan, H., Ni, P., Ou, G., Shen, K., Zhang, W., 2004. In: Fluid inclusion. Science Press, Beijing, pp. 1–486.

Mao, J., Kerrich, R., Li, H., Li, Y., 2002. High ³He/⁴He ratios in the Wangu gold deposit, Hunan province, China: implications for mantle fluids along the Tanlu deep fault zone. Geochem. J. 36 (3), 197–208.

Marty, B., Appora, I., Barrat, J.-A.A., Deniel, C., Vellutini, P., Vidal, P., 1993. He, Ar, Sr, Nd and Pb isotopes in volcanic rocks from Afar: evidence for a primitive mantle component and constraints on magmatic sources. Geochem. J. 27, 219–228.

McCrea, J.M., 1950. On the isotopic chemistry of carbonates and a paleotemperature scale. J. Chem. Phys. 18 (6), 849–857.

McCuaig, C.T., Kerrich, R., 1998. P—T—t—deformation—fluid characteristics of lode gold deposits: evidence from alteration systematics. Ore Geol. Rev. 12 (6), 381–453.

McKeag, S., Craw, D., 1989. Contrasting fluids in gold-bearing quartz vein systems formed progressively in a rising metamorphic belt, Otago Schist, New Zealand. Econ. Geol. 84 (1), 22–33.

Menzies, C.D., Teagle, D.A., Craw, D., Cox, S.C., Boyce, A.J., Barrie, C.D., Roberts, S., 2014. Incursion of meteoric waters into the ductile regime in an active orogen. Earth Planet. Sci. Lett. 399, 1–13.

Metcalfe, I., 2013. Gondwana dispersion and Asian accretion: tectonic and palaeogeographic evolution of eastern Tethys. J. Asian Earth Sci. 66, 1–33.

Nesbitt, B.E., 1988. Gold deposit continuum: a genetic model for lode Au mineralization in the continental crust. Geology 16 (11), 1044–1048.

O'Neil, J.R., 1986. Theoretical and experimental aspects of isotopic fractionation. Rev. Mineral. 16, 1–40.

Oberthuer, T., Mumm, A.S., Vetter, U., Simon, K., Amanor, J.A., 1996. Gold mineralization in the Ashanti Belt of Ghana; genetic constraints of the stable isotope geochemistry. Econ. Geol. 91 (2), 289–301.

Ohmoto, H., Rye, R.O., 1979. In: Isotopes of Sulfur and Carbon: Geochemistry of Hydrothermal Deposits. Wiley Interscience, New York, pp. 509–567.

Ohmoto, H., Goldhaber, M.B., 1997. In: Geochemistry of Hydrothermal Ore Deposits, third ed. John Willey and Sons, New York, pp. 17–611.

Pan, G., Wang, L., Li, R., Yuan, S., Ji, W., Yin, F., Zhang, W., Wang, B., 2012. Tectonic evolution of the Qinghai-Tibet Plateau. J. Asian Earth Sci. 53, 3–14.

Paytan, A., Gray, E.T., 2012. Sulfur isotope stratigraphy. In: Gradstein, F.M., Ogg, J.G., Schmitz, M. (Eds.), The Geologic Timescale 2012. Elsevier, Amsterdam, pp. 167–180.

Pei, Y., Yang, Z., Zhao, X., Zhang, X., Ma, W., Xu, Y., Mao, J., 2016. Sulfur and Lead Isotope Compositions of the Shangxu Orogenic Gold Deposit in Northern Tibet: implication for the Source of Ore-forming Material. Acta Geol. Sin. 90 (2), 341–351 (in Chinese with English Abstract).

Pei, Y., Yang, Z., Zhao, X., Zhang, X., Xu, Y., Ma, W., Mao, J., Zhuang, L., 2015. Genesis of the Shangxu Orogenic Gold Deposit in Northern Tibet: constrains from Fluid Inclusions and Isotopic Compositions. Acta Geol. Sin. 89 (10), 1814–1825.

Phillips, G.N., Hughes, M.J., 1996. The geology and gold deposits of the Victorian gold province. Ore Geol. Rev. 11 (5), 255–302.

Phillips, G.N., Nooy, D.D., 1988. High-grade metamorphic processes which influence Archaean gold deposits, with particular reference to Big Bell, Australia. J. Metamorph. Geol. 6 (1), 95–114.

Pitcairn, I.K., Craw, D., Teagle, D.A.H., 2014. The gold conveyor belt: large-scale gold mobility in an active orogen. Ore Geol. Rev. 62, 129–142.

Pitcairn, I.K., Teagle, D.A., Craw, D., Olivo, G.R., Kerrich, R., Brewer, T.S., 2006. Sources of metals and fluids in orogenic gold deposits: insights from the Otago and Alpine Schists, New Zealand. Econ. Geol. 101 (8), 1525–1546.

Poitrasson, F., 2017. Silicon isotope geochemistry. Rev. Mineral. Geochem. 82 (1), 289–344.

Qu, X., Wang, R., Xin, H., Jiang, J., Chen, H., 2012. Age and petrogenesis of A-type granites in the middle segment of the Bangonghu-Nujiang suture, Tibetan plateau. Lithos 146–147, 264–275.

Ridley, J.R., Diamond, L.W., 2000. Fluid chemistry of orogenic lode gold deposits and implications for genetic models. Econ. Geol. 13, 141–162.

Ryan, R., Smith, P., 1998. A review of the mesothermal gold deposits of the Meguma Group, Nova Scotia, Canada. Ore Geol. Rev. 13 (1–5), 153–183.

Sandiford, M., Keays, R. R., 1986, Structural and tectonic constraints on the origin of gold deposits in the Ballarat slate belt, Victoria, Turbidite-hosted gold deposits, Volume 32, Geological Association of Canada Special Paper, pp. 15–24.

Sangster, A.L., Smith, P.K., Goodfellow, W., 2007. Metallogenic summary of the Meguma gold deposits, Nova Scotia: mineral Deposits of Canada: a synthesis of major deposit-types, district metallogeny, the evolution of geological provinces, and exploration methods. In: Geological Association of Canada, Mineral Deposits Division, Special Publication, vol. 5, pp. 723–732.

Shen, J., Li, S., Santosh, M., Meng, K., Dong, G., Wang, Y., Yin, N., Ma, G., Yu, H., 2013. He–Ar isotope geochemistry of iron and gold deposits reveals heterogeneous lithospheric destruction in the North China Craton. J. Asian Earth Sci. 78, 237–247.

Shieh, Y., Taylor, H.P., 1969. Oxygen and carbon isotope studies of contact metamorphism of carbonate rocks. J. Petrol. 10, 307–331.

Simmons, S.F., Sawkins, F.J., Schlutter, D.J., 1987. Mantle-derived helium in two Peruvian hydrothermal ore deposits. Nature 329 (2), 429.

Song, Y., Tang, J., Qu, X., Wang, D., Xin, H., Yang, C., Lin, B., Fan, S., 2014. Progress in the study of mineralization in the Bangongco-Nujiang metallogenic belt and some new recognition. Adv. Earth Sci. 29 (7), 795–809 (in Chinese with English Abstract).

Song, Y., Zeng, Q., Liu, H., Liu, Z., Li, H., Dexiyangzong, 2019. An innovative perspective for the evolution of Bangong-Nujiang Ocean: also discussing the Paleo- and Neo-Tethys conversion. Acta Petrol. Sin. 35 (3), 625–641 (in Chinese with English Abstract).

Stuart, F.M., Burnard, P.G., Taylor, R.P., Turner, G., 1995. Resolving mantle and crustal contributions to ancient hydrothermal fluids: He-Ar isotopes in fluid inclusions from Dae Hwa W-Mo mineralisation, South Korea. Geochim. Cosmochim. Acta 59 (22), 4663–4673.

Stuart, F., Turner, G., Duckworth, R., Fallick, A.E., 1994. Helium isotopes as tracers of trapped hydrothermal fluids in ocean-floor sulfides. Geology 22.

Tang, J., Durji, Liu, H., Lang, X., Zhang, J., Zheng, W., Ying, L., 2012. Minerogenetic series of ore deposits in the east part of the Gangdise metallogenic belt. Acta Geosci. Sin. 33 (4), 393–410 (in Chinese with English Abstract).

Tang, J., Song, Y., Wang, Q., Lin, B., Yang, C., Guo, N., Fang, X., Yang, H., Wang, Y., Gao, K., Ding, S., Zhang, Z., Duan, J., Chen, H., Su, D., Feng, J., Liu, Z., Wei, S., He, W., Song, J., Li, Y., Wei, L., 2016. Geological characteristics and exploration model of the Tiegelongnan Cu (Au-Ag) deposit: the first ten million tons metal resources of a porphyry-epithermal deposit in Tibet. Acta Geosci. Sin. 37 (6), 663–690 (in Chinese with English Abstract).

Tang, J., Wang, Q., Yang, H., Gao, X., Zhang, Z., Zou, B., 2017. Mineralization, exploration and resource potential of porphyry-skarn-epithermal copper polymetallic deposits in Tibet. Acta Geosci. Sin. 38 (5), 571–613 (in Chinese with English Abstract).

Taylor, H., Barnes, H., 1997. Oxygen and hydrogen isotope relationships in hydrothermal mineral deposits. In: Geochemistry of Hydrothermal Ore Deposits, pp. 229–302.

Taylor Jr., H.P., Epstein, S., 1962. Relationship between O18/O16 ratios in coexisting minerals of igneous and metamorphic rocks: part 1: principles and experimental results. Geol. Soc. Am. Bull. 73 (4), 461–480.

Tolstikhin, I.N., 1978. A review-Some recent advances in isotope geochemistry of light rare gases. Adv. Earth Planet. Sci. 3, 33–62.

Welhan, J.A., 1988. Origins of methane in hydrothermal systems. Chem. Geol. 71 (1), 183–198.

Whiticar, M.J., 1999. Carbon and hydrogen isotope systematics of bacterial formation and oxidation of methane. Chem. Geol. 161 (1), 291–314.

Wong, K., Zhou, M., Chen, W.T., O'Brien, H., Lahaye, Y., Chan, S.-L.J., 2017. Constraints of fluid inclusions and in-situ S-Pb isotopic compositions on the origin of the North Kostobe sediment-hosted gold deposit, eastern Kazakhstan. Ore Geol. Rev. 81, 256–269.

Xiao, R., 2002, Research on Metallogenic Regularities and Prospecting of Gold Deposits at the Gaize District, Tibet: Doctoral Thesis, China University of Geosciences (Beijing), pp. 99 (in Chinese with English Abstract).

Xiao, W., Li, G., Huang, H., Ma, D., Zhang, Z., Quzha, 2013. Prospecting indicator and ore-controlling factors of Shangxu gold deposit in north Tibet. Gold 34 (10), 17–21 (in Chinese with English Abstract).

Xiao, W., Liu, H., Li, G., Huang, H., Ma, D., Zhang, Z., Yan, G., Zhang, H., 2017. Low to moderate temperature, low salinity and enrichment of CO2 hydrothermal fluid at Shangxu orogenic Gold Deposit in Shuanghu, Northern Xizang(Tibet): evidence from fluid inclusions, H-O isotopic composition. Geol. Rev. 63 (3), 793–808 (in Chinese with English Abstract).

Zeng, M., Chen, J., Wei, C., 2017. The Mugagangri Group is an accretionary complex accreted onto the south margin of Qiangtang. Earth Sci. Front. 24 (5), 207–217 (in Chinese with English abstract).

Zheng, S., Zhang, Z., Ni, B., Hou, F., Shen, M., 1982. Hydrogen and Oxygen Isotopic Studies of Thermal Water in Xizang. Acta Scientiarum Naturalium Universitatis Pekinensis 01, 99–106 (in Chinese with English Abstract).

Zheng, Y., 1999. Oxygen isotope fractionation in carbonate and sulfate minerals. Geochem. J. 33 (2), 109–126.

Zhou, T., Yuan, F., Yue, S., Liu, X., Zhang, X., Fan, Y., 2007. Geochemistry and evolution of ore-forming fluids of the Yueshan Cu–Au skarn- and vein-type deposits, Anhui Province, South China. Ore Geol. Rev. 31 (1), 279–303.

Zhu, D., Li, S., Cawood, P.A., Wang, Q., Zhao, Z., Liu, S., Wang, L., 2016. Assembly of the Lhasa and Qiangtang terranes in central Tibet by divergent double subduction. Lithos 245, 7–17.

Zhu, D., Zhao, Z., Niu, Y., Dilek, Y., Hou, Z., Mo, X., 2013. The origin and pre-Cenozoic evolution of the Tibetan Plateau. Gondwana Res. 23 (4), 1429–1454.